
Structured and Informed Probabilistic Modeling with the Thermodynamic Kolmogorov-Arnold Model

Prithvi Raj

Zettascale Computing Corp.*
prithvi@zettalaboratories.com

Abstract

We adapt the Kolmogorov–Arnold Representation Theorem to generative modeling by reinterpreting its inner functions as a Markov Kernel between probability spaces via inverse transform sampling. We present a generative model that is interpretable, easy to design, and efficient. Our approach couples a Kolmogorov–Arnold Network generator with independent energy-based priors, trained via Maximum Likelihood. Inverse sampling enables fast inference, while prior knowledge can be incorporated before training to better align priors with posteriors, thereby improving learning efficiency and sample quality. The learned prior is also recoverable and visualizable post-training, offering an empirical Bayes perspective. To address inflexibility and mitigate prior–posterior mismatch, we introduce scalable extensions based on mixture distributions and Langevin Monte Carlo methods, admitting a trade-off between flexibility and training efficiency. Our contributions connect classical representation theorems with modern probabilistic modeling, while balancing training stability, inference speed, and the quality and diversity of generations.

1 Introduction

The Thermodynamic Kolmogorov-Arnold Model (T-KAM) provides a solution to the problems posed by arbitrarily deep, uninformed neural networks by focusing on finite sums of continuous functions at the core of generative models.

Based on the latent space energy-based prior model introduced by Pang et al. [2020], we use the Kolmogorov–Arnold Representation Theorem, (KART by Givental et al. [2009]), to structure Maximum Likelihood Estimation (MLE) for dense Kolmogorov–Arnold Networks, (KANs presented by Liu et al. [2024]), where both the depth and width of layers are precisely determined by the data and latent dimensionalities.

While T-KAM can be extended to open-ended architectures, our initial focus adheres to KART in order to introduce structural bias and inform scaling alongside formulaic laws, such as those proposed by Kaplan et al. [2020]. This standardization may also benefit scientific modelling, where

architectural choices can otherwise influence the interpretation of experimental data.

Adherence to KART requires the use of KANs, which are well-suited to the recent hardware advances introduced by Zetta [2024]. This might support the broader adoption of T-KAM, enabling accessible design, principled scaling, and reduced dependence on automated tuning or heuristics.

Moreover, by expressing the lower-dimensional latent space with single-variable functions, our method improves latent space interpretability for domain experts who may not be well-versed in machine learning.

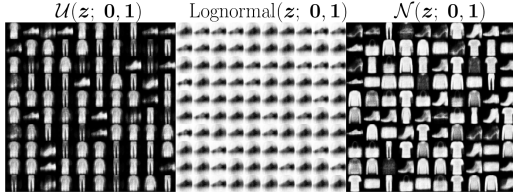
Firstly, T-KAM embodies an empirical Bayes approach, where latent priors are initialized from a reference distribution and updated throughout training. The latent distribution can follow either a conventional EBM or an exponential tilting operation, where each latent feature is initialized from a univariate reference prior. The former offers flexibility, while the latter imposes useful structure. We argue that careful selection of ref-

*previously Exa Laboratories, Inc.

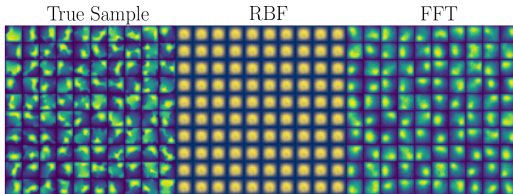
erence priors can improve training efficiency by better aligning the prior with the posterior before training commences, (Fig. 1a).

Additionally, we argue that the function-based nature of KART enables inductive biases to be leveraged by the model, (Fig. 1b). The flexibility in selecting basis functions or imposing functional constraints during training remains a compelling direction within the KAN research community. For instance, Fourier bases can introduce periodic biases, while Wavelet bases might be suited for spatial or temporal biases, as introduced by Xu et al. [2024] and Bozorgasl and Chen [2024], respectively. In this work, we use generic bases to maintain representational flexibility; however, domain-specific bases are expected to better align latent encodings with the data space.

By removing redundant expressivity in generic bases and EBM priors, otherwise required to capture the vastness of unspecific data manifolds, domain-specific bases can focus representation on physically meaningful features. Future directions may involve shaping these constituent functions to enforce governing equations while integrating observational data, similar to the physics-informed methods of Raissi et al. [2018].



(a) Generated FMNIST, (Xiao et al. [2017]), after just 2,000 parameter updates using MLE / IS adhering to KART’s structure. Uniform, lognormal, and Gaussian priors are contrasted using RBF bases by Li [2024].



(b) Darcy flow, (Li et al. [2021]), after 12,000 parameter updates using MLE / IS while adhering to KART. RBFs by Li [2024] are contrasted against FFTs by Xu et al. [2024] with lognormal priors.

Figure 1: Generative modeling using KART with different priors and basis functions. The middle image grids are coloured differently for clarity.

After training, the interpretable structure of KANs allows the recovery of latent priors via visualization or symbolic regression, as per the approach of Liu et al. [2024], (Fig. 2). For smaller-scale models, this can facilitate scientific discovery, support downstream tasks, and contribute to mechanistic interpretability research (reviewed by Bereska and Gavves [2024]).

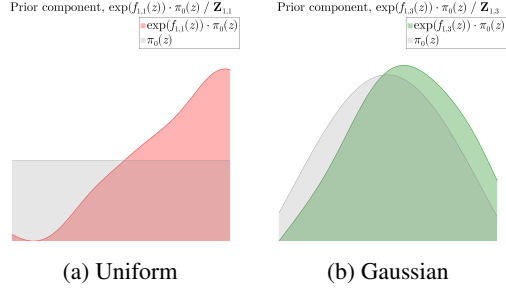


Figure 2: Three exponentially-tilted priors, extracted after training on MNIST (Deng [2012]) for 2,000 parameter updates using MLE / IS, while adhering to KART with RBFs. Lognormal is untrained due to posterior collapse.

These ideas define the baseline model, which adheres strictly to KART. In Sec. 2.4, we introduce practical strategies for scaling the univariate prior while relaxing KART’s constraints to address its potential inflexibility. We show how inter-dimensional relationships can be incorporated into the prior via a mixture distribution, enabling compatibility with ITS through a component-wise approach that preserves fast inference post-training.

We also explore replacing IS with the Unadjusted Langevin Algorithm (ULA), using the ideas of Brooks et al. [2011] and Roberts and Stramer [2002], and adopting the sampling strategy proposed in Pang et al. [2020]. Although ULA is more expensive than IS, it remains efficient due to the low dimensionality of the latent space. ULA is particularly well-suited to smooth, unimodal distributions and provides more exploration, which is valuable when the prior is high-dimensional and substantially misaligned with the posterior, which can compromise the reliability of the IS estimator.

In Sec.3, we propose an additional training criterion based on population-based Markov Chain Monte Carlo (pMCMC) methods, specifically Parallel Tempering (PT by Swendsen and Wang [1986]), to improve sampling performance in the presence of multimodal posteriors. While this method is more demanding, it targets the convergence issues often observed in EBMs.

Prior work addressing poor MCMC convergence in EBMs has typically relied on diffusion models, such as the hierarchical EBM by Cui and Han [2024] and the diffusion-assisted EBM by Zhang et al. [2023]. In contrast, our approach involves posterior annealing rather than denoising. Specifically, it decomposes the posterior into a sequence of power posteriors by Friel and Pettitt [2008], maintaining prior interpretability and enabling fast inference post-training. Although this may reduce expressivity compared to hierarchical EBMs, it ensures that inductive biases are easy to embed into the latent prior and retain during training.

Our criterion is derived from the discretized Thermodynamic Integral and the Steppingstone Estimator (SE), as described by Calderhead and Girolami [2009] and Annis et al. [2019]. This addresses concerns raised by Zhang et al. [2023] regarding the limited impact of PT on learning dynamics and parameter updates.

We evaluate these scalable extensions in Sec. 4.3, finding that the mixture prior outperforms a deep prior that is architecturally similar to the EBM used by Pang et al. [2020], while also offering greater computational efficiency. In contrast, the use of pMCMC and SE is not justified in our setting, given the significant computational overhead and limited gains. However, this assessment may change as better posterior sampling strategies become feasible with advances in hardware, such as those proposed by Zetta [2024].

To the best of our knowledge, this is the first application of a representation theorem to a probabilistic domain without compromising its deterministic structure. We introduce a practical and expressive framework for generative modelling, naturally suited to multimodal (multiple data type) tasks, as demonstrated by Yuan et al. [2024], and extendable to interpretable classification and text-to-text generation, following the principles of Pang and Wu [2021].

T-KAM also addresses a core limitation of the EBM prior framework proposed by Pang et al. [2020] by enabling inexpensive, yet high-quality inference through ITS, avoiding the computational overhead of iterative MCMC methods. Future work may further eliminate MCMC from training by incorporating amortized inference and variational methods, as guided by Kingma and Welling [2022]. This supports our claim that T-KAM can potentially support a sustainable life cycle in data-driven science and engineering, justified against previous findings by Wu et al. [2022] in Sec. A.3.

We present T-KAM as an initial step to inspire further adaptations of KART in machine learning. This work aims to lay the groundwork for more exploration amongst the research community, with the far-reaching hope of eventually advancing towards a broader conceptualization: *“The Kolmogorov-Arnold Representation Theorem Is All You Need.”*

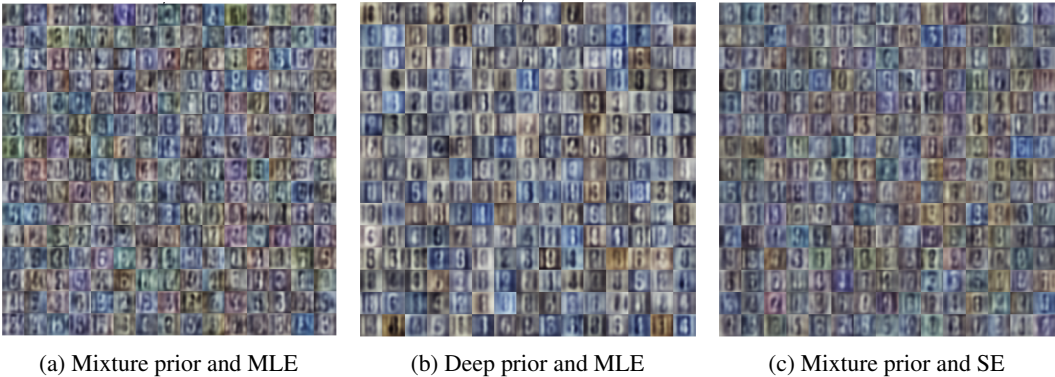


Figure 3: SVHN by Netzer et al. [2011], trained using the different scaling strategies for just 8,000 parameter updates. The priors are realized with Chebyshev bases by SS et al. [2024] from Gaussian reference distributions.

2 The Thermodynamic Kolmogorov-Arnold Model

This section introduces the model for Marginal Likelihood Estimation (MLE) along with a summary of the sampling procedures. More detailed sampling theory is provided in Sec. A.7.

2.1 Kolmogorov-Arnold theorem

The Kolmogorov–Arnold Representation theorem (KART) presented by Givental et al. [2009] forms the basis of T-KAM. A structured proof of the theorem has been provided by Dzhenzher and Skopenkov [2022]. For any integer $n_z > 1$, there are continuous univariate functions $\Phi_q : \mathbb{R} \rightarrow \mathbb{R}$ and $\psi_{q,p} : [0, 1] \rightarrow \mathbb{R}$, such that any continuous multivariate function, $g : [0, 1]^{n_z} \rightarrow \mathbb{R}$, can be represented as a superposition of those functions:

$$g(u_1, \dots, u_{n_z}) = \sum_{q=1}^{2n_z+1} \Phi_q \left(\sum_{p=1}^{n_z} \psi_{q,p}(u_p) \right), \quad (1)$$

2.2 Univariate energy-based prior

In T-KAM, $u_p \sim \mathcal{U}(u_p; 0, 1)$ is treated as a uniform random variable. The functions $\psi_{q,p}$ are interpreted as inverse cumulative distribution functions (CDFs) corresponding to independent univariate priors. These priors are defined over the probability space $(\mathcal{Z}, \mathcal{B}(\mathcal{Z}), \pi)$, where $\mathcal{Z} \subset \mathbb{R}$ denotes the latent space, $\mathcal{B}(\mathcal{Z})$ is the Borel σ -algebra on \mathcal{Z} , and π is a probability measure.

$$\psi_{q,p}(u_p) = F^{-1}(\pi_{q,p})(u_p), \quad (2)$$

where $F^{-1}(\pi_{q,p}) : [0, 1] \rightarrow \mathcal{Z}$ is the generalized inverse CDF associated with a parameterized latent distribution, $\pi_{q,p}$. This is valid under standard regularity assumptions on F , since it is a measurable, monotone, increasing function, and thus $F^{-1}(u) = \inf \{z \in \mathcal{Z} : F(z) \geq u\}$ is a measurable mapping between probability spaces:

$$([0, 1], \mathcal{B}([0, 1]), \mu) \xrightarrow{F^{-1}} (\mathcal{Z}, \mathcal{B}(\mathcal{Z}), \pi), \quad (3)$$

where μ is the Lebesgue measure on $[0, 1]$. This induces a deterministic pushforward measure via a Markov kernel from the uniform space to the latent space:

$$K(u_p, A) = \mathbf{1}_A(\psi_{q,p}(u_p)) = \delta_{\psi_{q,p}(u_p)}(A),$$

where δ_z denotes the Dirac measure centered at z . Consequently, the transformation $u_p \mapsto \psi_{q,p}(u_p)$ defines a valid sampling procedure for latent variables. We parameterize the latent distribution $\pi_{q,p}$ via exponential tilting of a base prior π_0 :

$$\pi_{q,p}(z) = \frac{\exp(f_{q,p}(z))}{Z_{q,p}} \pi_0(z), \quad (4)$$

where $f_{q,p}(z)$ is a learned energy function and $Z_{q,p}$ is the normalizing constant (partition function) that ensures $\pi_{q,p}$ defines a valid probability.

The inspiration for this exponential tilting form can be traced to the energy-based prior introduced by Pang et al. [2020], adapted to the univariate case. The base prior π_0 serves as a reference measure that guides the form of the learned distribution $\pi_{q,p}$, allowing for flexible reweighting via the energy function $f_{q,p}$.

For $\pi_{q,p}$ to define a valid probability distribution, it must satisfy countable additivity while being non-negative and normalized. This is guaranteed if $f_{q,p} : \mathcal{Z} \rightarrow \mathbb{R}$ is Borel-measurable and integrable with respect to the reference density π_0 , ensuring the finiteness of the partition function:

$$Z_{q,p} = \int_{\mathcal{Z}} \exp(f_{q,p}(z)) d\pi_0(z) < \infty. \quad (5)$$

In practice, $f_{q,p}$ can be parameterized in various ways, made possible by the recent development of Kolmogorov–Arnold Networks (KANs). For instance, smoothing splines, such as those used by Liu et al. [2024] or Bohra et al. [2020]. Splines are typically defined on bounded domains, allowing the support of $\pi_{q,p}$ to be explicitly controlled by the user.

The partition function $Z_{q,p}$ is often intractable in energy-based models. However, in this univariate setting, where the energy function is smooth and defined on a bounded domain $[z_{\min}, z_{\max}]$, it can be accurately approximated using Gauss–Kronrod quadrature Laurie [1997]:

$$\begin{aligned} Z_{q,p} &= \int_{z_{\min}}^{z_{\max}} \exp(f_{q,p}(z)) \pi_0(z) dz \\ &\approx \sum_{i=1}^{N_{\text{quad}}} w_i G(z_i^{\text{node}}), \end{aligned} \quad (6)$$

where $G(z) = \exp(f_{q,p}(z)) \pi_0(z)$, and $\{z_i^{\text{node}}, w_i\}_{i=1}^{N_{\text{quad}}}$ are the quadrature nodes and weights for the interval $[z_{\min}, z_{\max}]$. The smoothness of G , together with its bounded support, makes this approximation highly accurate.

With a valid form for the normalized CDF, inverse transform sampling (ITS) can be used to draw samples from $\pi_{q,p}$ as deterministic transformations of uniform noise. This preserves the deterministic structure of KART while enabling flexible, learnable latent distributions. Inverse transform sampling remains effective even for functions that are not Riemann integrable, provided they are integrable in the Lebesgue sense, typical for the functions in KAN literature.

As a result, the model retains a coherent probabilistic interpretation of KART that is consistent with the energy-based framework proposed by Pang et al. [2020], which is well suited to maximum likelihood training.

However, this approach is significantly limited, as it ignores inter-dimensional dependencies in the latent space and results in an axis-aligned joint distribution. We address this inflexibility in Sec. 2.4.2 by relaxing our adherence to KART.

2.3 Kolmogorov-Arnold Network generator

Having sampled the intermediary latent variable with ITS such that $z_{q,p} = F^{-1}(\pi_{q,p})(u_p)$, the generator, $\mathcal{G} : \mathcal{Z} \rightarrow \mathcal{X}$, is formulated by:

$$\begin{aligned} z_{q,p}^{(s)} &\sim \pi_{q,p}(z), \quad \text{and} \quad \epsilon_o^{(s)} \sim \mathcal{N}(0, \sigma_\epsilon^2), \\ \tilde{x}_o^{(s)} &= \sum_{q=1}^{2n_z+1} \Phi_{o,q} \left(\sum_{p=1}^{n_z} z_{q,p}^{(s)} \right) + \epsilon_o^{(s)}, \\ \tilde{\mathbf{x}}^{(s)} &= \begin{pmatrix} \sum_{q=1}^{2n_z+1} \Phi_{1,q} \left(\sum_{p=1}^{n_z} z_{q,p}^{(s)} \right) \\ \sum_{q=1}^{2n_z+1} \Phi_{2,q} \left(\sum_{p=1}^{n_z} z_{q,p}^{(s)} \right) \\ \vdots \\ \sum_{q=1}^{2n_z+1} \Phi_{n_x,q} \left(\sum_{p=1}^{n_z} z_{q,p}^{(s)} \right) \end{pmatrix} + \boldsymbol{\epsilon}^{(s)}, \end{aligned} \quad (7)$$

where $\tilde{\mathbf{x}}^{(s)} = \{\tilde{x}_o^{(s)}\}_{o=1}^{n_x}$ represents a generated data sample corresponding to a single latent sample indexed by s , n_x is used to specify the dimension of $\tilde{\mathbf{x}}^{(s)}$, and the noise is a Gaussian sample, $\epsilon_o^{(s)} \sim \mathcal{N}(\epsilon; \mathbf{0}, \sigma_\epsilon^2 \mathbf{I})$ with hyperparameter σ_ϵ . The functions, $\Phi_{o,q} : \mathbb{R} \rightarrow \mathbb{R}$, are realizable as basis or KAN functions similar to $f_{q,p} : \mathcal{Z} \rightarrow \mathbb{R}$.

2.4 Scaling T-KAM

The trainable components of the prior and inner functions are shared across the features of each input $\mathbf{x}^{(b)}$, while the outer generator functions remain separate for each output dimension. Specifically, the learnable functions are defined as:

$$\begin{aligned} \mathbf{f} &= \begin{pmatrix} (f_{1,1}, \dots, f_{1,n_z}) \\ (f_{2,1}, \dots, f_{2,n_z}) \\ \vdots \\ (f_{2n_z+1,1}, \dots, f_{2n_z+1,n_z}) \end{pmatrix}, \\ \Phi &= \begin{pmatrix} (\Phi_{1,1}, \dots, \Phi_{1,2n_z+1}) \\ (\Phi_{2,1}, \dots, \Phi_{2,2n_z+1}) \\ \vdots \\ (\Phi_{n_x,1}, \dots, \Phi_{n_x,2n_z+1}) \end{pmatrix}, \end{aligned} \quad (8)$$

where n_x denotes the dimensionality of the observed data.

From this point forward, we formulate our derivations over a multivariate probability space $(\mathcal{Z}, \mathcal{B}(\mathcal{Z}), P)$, where \mathcal{Z} no longer represents a subinterval of the real line, but rather a subspace of $\mathbb{R}^{(2n_z+1) \times n_z}$. The measure P defines a product distribution over the latent variables:

$$P(\mathbf{z} | \mathbf{f}) = \pi_{1,1} \otimes \dots \otimes \pi_{2n_z+1,n_z},$$

where each component $\pi_{j,k}$ is defined via exponential tilting, as introduced in Sec. 2.2. The full latent variable \mathbf{z} is a matrix-valued random variable composed of these independent elements:

$$\mathbf{z} = \begin{pmatrix} (z_{1,1}, z_{1,2}, \dots, z_{1,n_z}) \\ (z_{2,1}, z_{2,2}, \dots, z_{2,n_z}) \\ \vdots \\ (z_{2n_z+1,1}, z_{2n_z+1,2}, \dots, z_{2n_z+1,n_z}) \end{pmatrix}. \quad (9)$$

This generalizes the latent representation to a high-dimensional space.

2.4.1 Generator

The generator functions, $\Phi_{o,q}$, can be considered a separate generator network allowing for more flexible realizations, such as convolutional layers when adherence to Eq. 1 is not required. Deepening this generator, as guided by Liu et al. [2024] for the Kolmogorov-Arnold Network (KAN), does not replace KART as the innermost foundation of T-KAM:

$$\begin{aligned} x_o^{(s)} &= \sum_{l_n=1}^{L_n} h_{o,l_n} \left(\dots h_{l_3,l_2} \left(\sum_{l_1=1}^{L_1} h_{l_2,l_1} \right. \right. \\ &\quad \left. \left. \left(\sum_{q=1}^{2n_z+1} \Phi_{l_1,q} \left(\sum_{p=1}^{n_z} z_{q,p}^{(s)} \right) \right) \right) \right) + \epsilon_o^{(s)}. \end{aligned} \quad (10)$$

Here, each h represents a hidden layer introduced between the outer sum of Eq. 1, and the output feature space to allow for more expressivity when required. In fact, each successive instance of h can be interpreted as a distinct outer sum of Eq. 1, where the inner sum corresponds to the previous layer. This is valid provided that:

$$\begin{aligned} L_1 &= 2(2n_z + 1) + 1, \\ L_2 &= 2L_1 + 1, \\ &\vdots \\ L_n &= 2L_{n-1} + 1. \end{aligned} \quad (11)$$

Thus, a smooth transition between the latent space and data space can be achieved by progressively doubling layer widths, eliminating the need for arbitrary choices while maintaining relaxed compliance with KART.

Strict adherence to KART can be achieved for hidden layer $h_{l_k, l_{k-1}}$ by applying either a sigmoid or affine transformation after layer $h_{l_{k-2}, l_{k-3}}$ to shift its range back to $[0, 1]^{L_{k-1}}$. However, using sigmoid may lead to vanishing gradients and we contend that function domains are less critical to KART than its structural properties and should not be prioritized over maintaining gradient flow and avoiding saturation.

Adopting a KAN-based generator also allows for training with L1 regularization, followed by pruning with the method proposed by Liu et al. [2024]. This enables further model compression beyond the baseline structure defined by KART.

2.4.2 Mixture prior

As noted in Sec. 2.2, the independence of the priors $\pi_{q,p}$ limits expressivity. Moreover, the summation over p in Eq. 7 accumulates the variances of sampled $z_{q,p}$, which can lead to overly diffuse representations. To address this, particularly for more complex generative tasks such as those in Sec. 4.3, we relax the strict adherence to KART by reformulating the prior as a mixture distribution. This involves moving the summation over p out of the generator and absorbing it into the prior, yielding a mixture model:

$$\sum_{p=1}^{n_z} \pi_{q,p}(z) = \sum_{p=1}^{n_z} \alpha_{q,p} \frac{\exp(f_{q,p}(z))}{Z_{q,p}} \pi_0(z),$$

where $\sum_{p=1}^{n_z} \alpha_{q,p} = 1, \quad \alpha_{q,p} \geq 0.$ (12)

Here, $\alpha_{q,p}$ denote mixture weights, practically enforced via a softmax function. The resulting distribution defines a mixture of energy-based priors. Sampling becomes more efficient than in the previous formulation, as it proceeds component-wise using ITS for discrete variables, following Devroye [2006]. However, this violates strict adherence to KART, since F now corresponds to a discrete rather than continuous CDF.

To encourage balanced weighting and reduce model complexity, L1 regularization can be ap-

2.5 Maximum likelihood training

With N_x training examples in a batch, the optimization objective is the minimization of the negative log-marginal likelihood:

$$\min_{\mathbf{f}, \Phi} \mathcal{L}(\mathbf{x}^{(1)}, \dots, \mathbf{x}^{(N_x)}) = \min_{\mathbf{f}, \Phi} \left[- \sum_{b=1}^{N_x} \log \left(P(\mathbf{x}^{(b)} | \mathbf{f}, \Phi) \right) \right]. \quad (15)$$

The conditional dependency on the collection, \mathbf{f}, Φ , represents all learnable elements of T-KAM. For each sample of $\mathbf{x}^{(b)}$, the log-marginal likelihood in Eq. 15 can be separated out into two log-distributions by first introducing the latent vector, \mathbf{z} , otherwise absent upon marginalization over the

plied to $\alpha_{q,p}$ and small values can be pruned. The mixture proportions are learned by adding $\log \alpha_{q,p}$ to the gradients of the prior in Sec. 2.5.1.

Component selection follows a categorical distribution over $p = 1, \dots, n_z$, determined by $\alpha_{q,p}$. Let $u_{\text{mix}} \sim \mathcal{U}(u_{\text{mix}}; 0, 1)$. Guided by Devroye [2006] regarding how ITS applied to discrete variables, the selected component p^* is given by:

$$p^* = \min \left\{ j \mid \sum_{p=1}^j \alpha_{q,p} \geq u_{\text{mix}} \right\}. \quad (13)$$

This ensures that each component p^* is selected with probability α_{q,p^*} . ITS can then be used to sample from the chosen component, (see 2.6.1).

2.4.3 KAN prior

If required, we may further deepen the energy functions $f_{q,p}$ using the KAN approach. In fact, each $f_{q,p}$ can itself be a realization of Eq. 1 when its domain is restricted to $[0, 1]$. This extension introduces new challenges:

1. It reduces the interpretability of the prior, complicating the recovery and visualization of trained priors.
2. It compromises the component-wise or univariate structure of the prior, undermining the validity of ITS and KART.

Instead, we propose removing the summation over p in Eq. 7 and reparameterizing the prior using a multilayer KAN energy function, which can be deepened as needed:

$$P(\mathbf{z} | \mathbf{f}) = \frac{\exp \left(\sum_{q=1}^{2n_z+1} \Psi_{q,p} \left(\sum_{p=1}^{n_z} f_{q,p}(z) \right) \right)}{\mathcal{Z}} \pi_0(\mathbf{z}), \quad (14)$$

where $\mathbf{z} \in \mathcal{Z} \subset \mathbb{R}^{n_z}$, and is constrained to $[0, 1]^{n_z}$ when strict adherence to KART is required. Sampling from this prior can be carried out using the Unadjusted Langevin Algorithm (ULA), as described in Sec. 3.4.

latent distribution. This is shown under Sec. A.6.2, and the resulting expectation exhibits a lack of dependence on sampling, as proven under Sec. A.6.3:

$$\nabla_{\mathbf{f}, \Phi} \left[\log P(\mathbf{x}^{(b)} | \mathbf{f}, \Phi) \right] = \mathbb{E}_{P(\mathbf{z} | \mathbf{x}^{(b)}, \mathbf{f}, \Phi)} \left[\nabla_{\mathbf{f}} [\log P(\mathbf{z} | \mathbf{f})] + \nabla_{\Phi} \left[\log P(\mathbf{x}^{(b)} | \mathbf{z}, \Phi) \right] \right], \quad (16)$$

2.5.1 Log-prior

Given the independence of the prior’s parameters, the log-prior can be modeled as a sum over the univariate cases:

$$\log \left(P(\mathbf{z} | \mathbf{f}) \right) = \sum_{q=1}^{2n_z+1} \sum_{p=1}^{n_z} \log(\pi_{q,p}(z_{q,p})) = \sum_{q=1}^{2n_z+1} \sum_{p=1}^{n_z} f_{q,p}(z_{q,p}) + \log(\pi_0(z_{q,p})) - \log(Z_{q,p}) \quad (17)$$

Tractable normalization is available through Eq. 6, however it may be more efficient to discard normalization in the learning gradient. In Sec. A.6.4, we derive the contrastive divergence learning gradient for T-KAM, which is faster to train and more typical of energy-based modeling:

$$\begin{aligned} \mathbb{E}_{P(\mathbf{z} | \mathbf{x}, \mathbf{f}, \Phi)} \left[\nabla_{\mathbf{f}} [\log P(\mathbf{z} | \mathbf{f})] \right] &= \mathbb{E}_{P(\mathbf{z} | \mathbf{x}, \mathbf{f}, \Phi)} \left[\nabla_{\mathbf{f}} \sum_{q=1}^{2n_z+1} \sum_{p=1}^{n_z} f_{q,p}(z_{q,p}) \right] \\ &- \mathbb{E}_{P(\mathbf{z} | \mathbf{f})} \left[\nabla_{\mathbf{f}} \sum_{q=1}^{2n_z+1} \sum_{p=1}^{n_z} f_{q,p}(z_{q,p}) \right]. \end{aligned} \quad (18)$$

Here, \mathbf{z} is sampled from $P(\mathbf{z} | \mathbf{f})$ and $P(\mathbf{z} | \mathbf{x}^{(b)}, \mathbf{f}, \Phi)$ and reflects a univariate element of the prior model, (vectorized in Eq. 9). The expectation with respect to the posterior can be approximated using Importance Sampling (IS), outlined under Secs. 2.6.2 & A.7.2, or a standard Monte Carlo estimator when using Langevin sampling methods. The prior expectation may always be approximated with a Monte Carlo estimator taken across samples:

$$\mathbb{E}_{P(\mathbf{z} | \mathbf{f})} \left[\nabla_{\mathbf{f}} \sum_{q=1}^{2n_z+1} \sum_{p=1}^{n_z} f_{q,p}(z_{q,p}) \right] \approx \frac{1}{N_s} \sum_{s=1}^{N_s} \nabla_{\mathbf{f}} \sum_{q=1}^{2n_z+1} \sum_{p=1}^{n_z} f_{q,p}(z_{q,p}^{(s)}) \quad \text{where } z_{q,p}^{(s)} \sim \pi_{q,p}(z). \quad (19)$$

The gradient of Eq. 18 can therefore be viewed as a element-wise correction to the prior, incorporating information from the observations to align the prior with the posterior, thereby following the philosophy of empirical Bayes. The gradient can then be evaluated via autodifferentiation.

2.5.2 Log-likelihood

Depending on the task the log-likelihood can be modeled in multiple ways. For example, a Gaussian model might be adopted for images, and an autoregressive model for text. It can also be realized into a multimodal generative modeling framework using the principles outlined by Yuan et al. [2024].

$$\log \left(P(\mathbf{x}^{(b)} | \mathbf{z}, \Phi) \right) = \begin{cases} -\frac{\|\mathbf{x}^{(b)} - \tilde{\mathbf{x}}\|_2^2}{2\sigma_{\text{llhood}}^2} + \text{const}, & \text{(static continuous data)} \\ \sum_{o=1}^{n_x} \sum_{c=1}^K x_{o,c}^{(b)} \log \tilde{x}_{o,c} + \text{const}, & \text{(static discrete data)} \\ \sum_{t=1}^T \log \left(P(\mathbf{x}^{(b,t)} | \mathbf{x}^{(b,1)}, \dots, \mathbf{x}^{(b,t-1)}, \mathbf{z}, \Phi) \right), & \text{(sequential data)} \end{cases} \quad (20)$$

Here, $\tilde{\mathbf{x}}$ is a generated sample from Eq. 7 corresponding to a single batch item, $\mathbf{x}^{(b)}$, σ_{llhood} is a hyperparameter subject to assumptions regarding the variance of the data, and K denotes the number of discrete classes. The learning gradient attributed to the log-likelihood can also be evaluated using autodifferentiation, after first approximating the posterior expectation with IS or MC estimators.

2.6 Sampling procedures

There are two cases in T-KAM where samples are drawn from distributions that do not offer a means of sampling supported by off-the-shelf frameworks. Differentiability does not need to be maintained given the lack of gradient dependence on sampling, proven under Sec. A.6.3.

1. In Eqs. 7 & 19, $z_{q,p}$ is drawn from $\pi_{q,p}$ with inverse transform sampling (ITS).
2. The log-marginal likelihood and its learning gradient presented in Eqs. 15 & 16, involve expectations with respect to the posterior $P(\mathbf{z} | \mathbf{x}^{(b)}, \mathbf{f}, \Phi)$, which is potentially multimodal and complex. We propose Importance Sampling (IS) as an efficient method for estimating its expectation.

IS provides a quick approximation of the posterior expectation without requiring extensive exploration. In contrast, PT with ULA, (introduced in Sec. 3.4) is more stochastic and exploratory, often yielding higher-quality samples from the posterior.

A more comprehensive overview of the sampling methods is presented in Sec. A.7. The main body solely presents the summarized procedures.

2.6.1 Inverse transform sampling

To sample from a component of the latent distribution, $\pi_{q,p}$, we use inverse transform sampling (ITS), made possible given the unique characteristics of T-KAM. Specifically, the univariate, finite-grid structure of the constituent functions enables quadrature/interpolating integral approximations.

1. **CDF inversion:** Sampling occurs using the inverse cumulative distribution function (CDF): The CDF for a single component, $F_{\pi_{q,p}}$, is:

$$F_{\pi_{q,p}}(z') = \frac{\int_{z_{\min}}^{z'} \exp(f_{q,p}(z)) \pi_0(z) dz}{Z_{q,p}},$$

$$Z_{q,p} = \int_{z_{\min}}^{z_{\max}} \exp(f_{q,p}(z)) \pi_0(z) dz. \quad (21)$$

These two integrals can be conveniently and efficiently approximated using Gauss-Kronrod quadrature, (Laurie [1997]), given that $f_{q,p}$ is univariate and defined on a bounded grid:

$$G(z) = \exp(f_{q,p}(z)) \pi_0(z), \quad (22)$$

$$\int_{z_{\min}}^{z'} G(z) dz \approx \sum_{i=1}^{N_{\text{quad}}} w_i G(z_i^{\text{node}}), \quad (23)$$

where z_i^{node} and w_i are the Gauss-Legendre quadrature nodes and weights for the interval $[z_{\min}, z']$. A random variable is uniformly drawn and shared across q , $u_p \sim \mathcal{U}(u_p; 0, 1)$. The first interval where $F_{\pi_{q,p}}(z)$ is greater than u_p scaled by $Z_{q,p}$ is identified:

$$k^* = \min \left\{ j \mid \sum_{i=1}^j w_i G(z_i^{\text{node}}) \geq Z_{q,p} \cdot u_p \right\}. \quad (24)$$

2. **Linear interpolation:** The sample z_p is interpolated within the subset, $[z_{k^*-1}^{\text{node}}, z_{k^*}^{\text{node}}]$:

$$z_p \approx z_{k^*-1}^{\text{node}} + (z_{k^*}^{\text{node}} - z_{k^*-1}^{\text{node}}) \cdot \delta$$

$$\delta = \frac{u_p - F_{\pi_{q,p}}(z_{k^*-1}^{\text{node}})}{F_{\pi_{q,p}}(z_{k^*}^{\text{node}}) - F_{\pi_{q,p}}(z_{k^*-1}^{\text{node}})}. \quad (25)$$

The procedure ensures unbiased, high-quality, and efficient generation of samples, $z_{q,p}$, distributed according to $\pi_{q,p}$. It can be vectorized to generate samples from all prior elements.

2.6.2 Importance Sampling

The following procedure is elaborated in more detail under Sec. A.7.2. To approximate expectations with respect to the target, $P(\mathbf{z} | \mathbf{x}^{(b)}, \mathbf{f}, \Phi)$, we use Importance Sampling (IS).

1. **Proposal distribution:** N_s independent samples, $\{\mathbf{z}^{(s)}\}_{s=1}^{N_s}$, are drawn from the proposal distribution, $Q(\mathbf{z}) = P(\mathbf{z} | \mathbf{f})$, which the target distribution, $P(\mathbf{z} | \mathbf{x}^{(b)}, \mathbf{f}, \Phi)$ must be absolutely continuous with respect to. Sampling from Q is tractable with the procedure outlined in Sec. 2.6.1.
2. **Importance weights:** The normalized importance weights are evaluated:

$$w_{\text{norm}}(\mathbf{z}^{(s)}) = \frac{w(\mathbf{z}^{(s)})}{\sum_{r=1}^{N_s} w(\mathbf{z}^{(r)})}$$

$$= \text{softmax}_s \left(\log(P(\mathbf{x}^{(b)} | \mathbf{z}^{(s)}, \Phi)) \right). \quad (26)$$

3. **Effective Sample Size:** To prevent weight degeneracy, resampling is conducted when the Effective Sample Size (ESS) falls below a threshold specified by a hyperparameter, γ :

$$ESS = \frac{1}{\sum_{s=1}^{N_s} w_{\text{norm}}(\mathbf{z}^{(s)})} < \gamma \cdot N_s. \quad (27)$$

Otherwise, the weights are taken without alteration, (i.e. the next step is skipped). When the weights are uniformly spread the ESS evaluates to N_s . High-variance weights with a low

ESS indicate that many samples contribute minimally, resulting in inefficient sampling. Resampling focuses learning on samples that are more representative of the posterior distribution, thereby maximizing the usefulness of each parameter update.

4. **Resample:** If required, the population, $\{\mathbf{z}^{(s)}, w_{\text{norm}}(\mathbf{z}^{(s)})\}_{s=1}^{N_s}$, is resampled from. There are multiple ways to accomplish this, as compared by Douc et al. [2005]. Systematic, stratified, and residual resampling are provided in the codebase under Sec. A.1, parallelized on the CPU. In this study, we adopted residual resampling, (explained under Sec. A.7.3).
5. **Expectation estimation:** The posterior expectation of an arbitrary function $\rho(\mathbf{z})$, (e.g.,

the log-likelihood), is estimated with a Monte Carlo estimator:

$$\mathbb{E}_{P(\mathbf{z}|\mathbf{x}^{(b)}, \mathbf{f}, \Phi)}[\rho(\mathbf{z})] \approx \sum_{s=1}^{N_s} \rho(\mathbf{z}_{\text{resampled}}^{(s)}) \cdot w_{\text{norm}}(\mathbf{z}_{\text{resampled}}^{(s)}). \quad (28)$$

This estimator is used for computing the log-marginal likelihood and its gradient in Eqs. 15 and 16. However, unlike ULA (discussed in Sec. 3.4 and demonstrated in Sec. 4.3), IS fails to support posterior exploration when the prior is poorly aligned, making it unsuitable for general-purpose tasks beyond those similar to the datasets presented in Secs. 4.1 and 4.2.

3 Steppingstone Estimator

This section explores the Steppingstone Estimator (SE) and Thermodynamic Integration (TI) as an alternative means of training T-KAM and estimating the marginal likelihood.

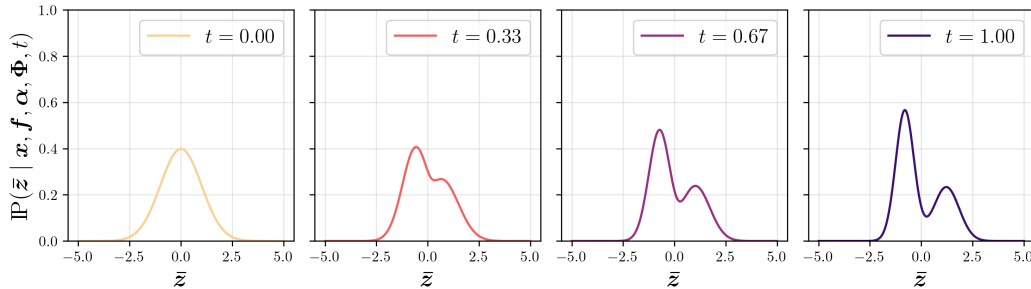


Figure 4: Demonstration of power posterior evolution with t . A simple Gaussian prior is sculpted into forms that resemble a more complex, multi-modal posterior as t is incremented from 0 to 1.

3.1 The Thermodynamic Integral

We inform our approach to tempering using the Thermodynamic Integral. In place of the log-marginal likelihood outlined in Eq. 15, this exploits the following representation derived in Sec. A.6.5:

$$\log \left(P(\mathbf{x}^{(b)} | \mathbf{f}, \Phi) \right) = \int_0^1 \mathbb{E}_{P(\mathbf{z}|\mathbf{x}^{(b)}, \mathbf{f}, \Phi, t)} \left[\log \left(P \left(\mathbf{x}^{(b)} | \mathbf{z}, \Phi \right) \right) \right] dt \quad (29)$$

Here, $P(\mathbf{z} | \mathbf{x}^{(b)}, \mathbf{f}, \Phi, t)$ has been introduced as the power posterior, which can be considered a representation of the original posterior distribution, with a likelihood tempered by a temperature parameter, t . This is introduced by Friel and Pettitt [2008] and organized for our purposes as follows:

$$P(\mathbf{z} | \mathbf{x}^{(b)}, \mathbf{f}, \Phi, t) = \frac{P(\mathbf{x}^{(b)} | \mathbf{z}, \Phi)^t \cdot P(\mathbf{z} | \mathbf{f})}{Z_t},$$

$$\text{where } Z_t = \mathbb{E}_{P(\mathbf{z}|\mathbf{f})} \left[P \left(\mathbf{x}^{(b)} | \mathbf{z}, \Phi \right)^t \right] = \int_{\mathcal{Z}} P \left(\mathbf{x}^{(b)} | \mathbf{z}, \Phi \right)^t dP(\mathbf{z} | \mathbf{f}) \quad (30)$$

Given the form of Eq. 30, setting $t = 0$ results in the power posterior distribution assuming the form of the prior distribution. As t increments, the posterior gradually adopts a shape more closely

resembling the true Bayesian posterior measure. At $t = 1$, the posterior recovers its original form and converges to the original posterior distribution.

The effect of tempering is illustrated in Fig. 4, starting with a Gaussian prior that is entirely uninformed of $\mathbf{x}^{(b)}$. As t increases from 0 to 1, the contribution of the likelihood term in Eq. 30 progressively grows, ultimately leading to the posterior at $t = 1$. This final posterior can be interpreted as the prior updated by information from the samples of $\mathbf{x}^{(b)}$.

3.2 Discretizing the Thermodynamic Integral

The exact calculation of the integral in Eq. 29 is feasible given that the bounds are $t = 0$, corresponding to the expectation being taken with respect to the prior, and $t = 1$, where it is taken with respect to the posterior. However, the integral can also be expressed exactly without collapsing the temperatures, offering greater flexibility in how the integral evolves through the temperature schedule, $\{t_k\}_{k=0}^{N_t}$. In particular, the temperature schedule is discretized as:

$$\mathbf{t} = (t_0, t_1, \dots, t_{N_t}), \quad t_k \in [0, 1] \quad (31)$$

Here, t_k denotes the tempering at the k -th index of the schedule, and N_t is the number of temperatures. As derived by Calderhead and Girolami [2009], Eq. 29 can then be evaluated using:

$$\log \left(P(\mathbf{x}^{(b)} \mid \mathbf{f}, \Phi) \right) = \frac{1}{2} \sum_{k=1}^{N_t} \Delta t_k (E_{k-1} + E_k) + \frac{1}{2} \sum_{k=1}^{N_t} D_{\text{KL}}(P_{t_{k-1}} \parallel P_{t_k}) - D_{\text{KL}}(P_{t_k} \parallel P_{t_{k-1}}) \quad (32)$$

Where:

$$\begin{aligned} \Delta t_k &= t_k - t_{k-1}, & E_k &= \mathbb{E}_{P(\mathbf{z} \mid \mathbf{x}^{(b)}, \mathbf{f}, \Phi, t_k)} \left[\log \left(P(\mathbf{x}^{(b)} \mid \mathbf{z}, \Phi) \right) \right], \\ D_{\text{KL}}(P_{t_{k-1}} \parallel P_{t_k}) &= \mathbb{E}_{P(\mathbf{z} \mid \mathbf{x}^{(b)}, \mathbf{f}, \Phi, t_{k-1})} \left[\log \left(\frac{P(\mathbf{z} \mid \mathbf{x}^{(b)}, \mathbf{f}, \Phi, t_{k-1})}{P(\mathbf{z} \mid \mathbf{x}^{(b)}, \mathbf{f}, \Phi, t_k)} \right) \right] \end{aligned} \quad (33)$$

This reflects the trapezium rule for numerical integration, supported by bias correction to provide an estimate of the Riemann integral that is especially robust to error. The learning gradient derived from the discretized Thermodynamic Integral is unchanged from the MLE gradient in Eq. 16, as demonstrated under Sec. A.6.6.

3.3 Steppingstone Estimator

In Sec. A.6.6, the Steppingstone estimator (SE) introduced by Annis et al. [2019] is derived from the discretized Thermodynamic Integral, thus establishing a connection between the two:

$$\log \left(P(\mathbf{x}^{(b)} \mid \mathbf{f}, \Phi) \right) = \sum_{k=1}^{N_t} \log \left(\frac{\mathbf{Z}_{t_k}}{\mathbf{Z}_{t_{k-1}}} \right) = \sum_{k=1}^{N_t} \left(\log(\mathbf{Z}_{t_k}) - \log(\mathbf{Z}_{t_{k-1}}) \right) = \underbrace{\log(\mathbf{Z}_{t_{N_t}})}_{=\text{MLE}} - \underbrace{\log(\mathbf{Z}_{t_0})}_{=0 \text{ (Eq. 40)}}. \quad (34)$$

Following the work of Annis et al. [2019], the log-partition ratios are estimated with Monte Carlo estimators using the intermediary samples of ULA:

$$\begin{aligned} \log \left(P(\mathbf{x}^{(b)} \mid \mathbf{f}, \Phi) \right) &= \log(\mathbf{Z}_{t_{N_t}})^{\text{SS}} = \sum_{k=1}^{N_t} \log \left(\frac{\mathbf{Z}_{t_k}}{\mathbf{Z}_{t_{k-1}}} \right) \\ &\approx \frac{1}{N_s} \sum_{k=1}^{N_t-1} \sum_{s=1}^{N_s} (t_{k+1} - t_k) \left[\log P \left(\mathbf{x}^{(b)} \mid \mathbf{z}^{(s, t_k)}, \Phi \right) \right], \quad \text{where } \mathbf{z}^{(s, t_k)} \sim P(\mathbf{z} \mid \mathbf{x}^{(b)}, \mathbf{f}, \Phi, t_k) \end{aligned} \quad (35)$$

SE and its variants, such as Annealed Importance Sampling (AIS) by Neal [1998], are commonly used to estimate a model's evidence without a tractable way to learn the prior, as they lack dependence on prior gradients beyond sampling. However, by recognizing the direct connection between the SE

and MLE learning gradients, as proven in Sec. A.6.6, one can simply add the contrastive divergence learning gradient from Eq. 18 to the SE estimator.

This is valid because the SE gradient matches the MLE gradient, and the likelihood gradient is independent of the prior gradient. The posterior expectation of contrastive divergence in Eq. 18 can be estimated with a Monte Carlo estimator using the final samples of ULA.

3.4 Unadjusted Langevin Algorithm (ULA) and Replica Exchange

In their implementation of Thermodynamic Integration (TI), Calderhead and Girolami [2009] estimated the Thermodynamic Integral using the discretization in Sec. 3.2, using population-based MCMC and Parallel Tempering (PT) to simultaneously sample from all power posteriors, as described by Swendsen and Wang [1986], Marinari and Parisi [1992], and Hukushima and Nemoto [1996].

Specifically, parallel chains were maintained at each temperature, (or Replica), using Metropolis-Hastings (MH by Metropolis and Ulam [1949]), to drive local moves for each power posterior. They also proposed a geometric path between the prior and posterior, enabling global swaps between adjacent temperatures. This approach allowed higher temperatures to leverage the efficient mixing of lower temperatures, thereby facilitating a more thorough exploration of the posterior landscape.

We adopt a similar strategy but follow Pang et al. [2020] in using the Unadjusted Langevin Algorithm (ULA) without MH correction, detailed by Brooks et al. [2011]. Specifically, we update samples using the forward Euler–Maruyama discretization of the Langevin SDE, as proposed by Roberts and Stramer [2002], with the transition kernel described in Sec. A.7.4:

$$\mathbf{z}^{(i+1, t_k)} = \mathbf{z}^{(i, t_k)} + \eta \nabla_{\mathbf{z}^{(i, t_k)}} \log \gamma \left(\mathbf{z}^{(i, t_k)} \right) + \sqrt{2\eta} \boldsymbol{\epsilon}^{(i, t_k)}, \quad (36)$$

where η is the step size, $\boldsymbol{\epsilon}^{(i, t_k)} \sim \mathcal{N}(\mathbf{0}, \mathbf{I})$, and γ_{t_k} denotes the target power posterior:

$$\log \gamma \left(\mathbf{z}^{(i, t_k)} \right) = \log P(\mathbf{z}^{(i, t_k)} \mid \mathbf{x}^{(b)}, \mathbf{f}, \Phi, t_k) \propto t_k \log P(\mathbf{x}^{(b)} \mid \mathbf{z}^{(i, t_k)}, \Phi) + \log P(\mathbf{z}^{(i, t_k)} \mid \mathbf{f}).$$

Unlike MCMC methods that solely rely on MH proposals, ULA accounts for the local geometry of the posterior, allowing more efficient exploration. In contrast, MH neglects this geometry, leading to high rejection rates, particularly problematic for the complex likelihood models used in T-KAM (Eq. 20), and requiring many iterations to sufficiently evolve the chain.

While ULA is computationally efficient and enables more flexible chain dynamics, it does not preserve detailed balance or reversibility. These can be recovered by incorporating MH corrections via the Metropolis-adjusted Langevin Algorithm (MALA by Rosicky et al. [1978]). The codebase optionally supports MALA with locally adaptive step-size tuning, (autoMALA by Biron-Lattes et al. [2024]), to assist when a single step size is not sufficient for all power posteriors. The algorithms are discussed under Secs. A.7.4 and A.7.5.

Nevertheless, ULA remains the preferred method in our work, motivated by its demonstrated efficiency and effectiveness by Pang et al. [2020], and further supported by the findings of Nijkamp et al. [2019b] and Nijkamp et al. [2019a], with regards to how short-run, biased MCMC methods can still be highly effective for sampling from EBMs.

ULA is best suited for smooth, unimodal distributions, but annealing with power posteriors might improve sampling from multimodal distributions. Mixing can be further improved by periodically enabling global swaps between adjacent temperatures, subject to the following acceptance criteria:

$$r = \frac{P(\mathbf{x}^{(b)} \mid \mathbf{z}^{(i, t_{k+1})}, \Phi)^{t_k} P(\mathbf{x}^{(b)} \mid \mathbf{z}^{(i, t_k)}, \Phi)^{t_{k+1}}}{P(\mathbf{x}^{(b)} \mid \mathbf{z}^{(i, t_k)}, \Phi)^{t_k} P(\mathbf{x}^{(b)} \mid \mathbf{z}^{(i, t_{k+1})}, \Phi)^{t_{k+1}}} \quad (37)$$

The proposed swap is accepted with probability: $\min(1, r)$, such that $\mathbf{z}^{(i, t_{k+1})} \leftrightarrow \mathbf{z}^{(i, t_k)}$.

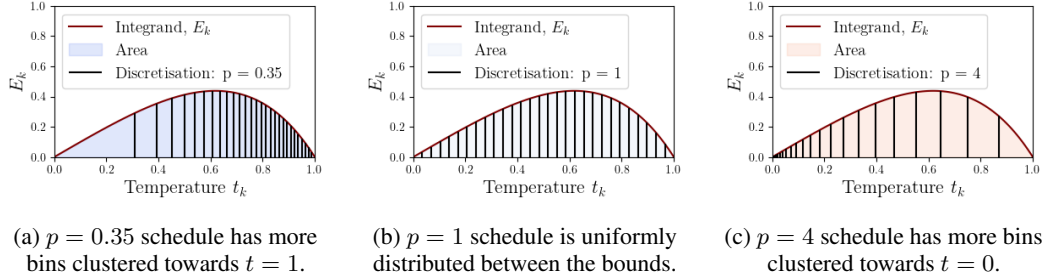


Figure 5: Plots depicting how the power-law schedule clusters integral approximation error. Evaluation points can be skewed towards a particular bound by choosing p . Increasing p provides more tempering, concentrating more evaluation points on smoother likelihoods. Tempering helps to mitigate practical challenges associated with the non-smoothness of the univariate functions in Eq. 1.

3.5 Cyclic annealing

Calderhead and Girolami [2009] demonstrated that uniformly scheduling the discretized temperatures in Eq. 31 results in unequal contributions of adjacent power posteriors to the Thermodynamic Integral. The success of TI and SE, relies on selecting each t_k to ensure sufficient overlap of adjacent power posteriors.

This overlap ensures a well-conditioned Radon-Nikodym derivative between adjacent power posteriors, as introduced in Sec. A.7.2, which influences the Monte Carlo estimator in Eq. 35, given that SE is an application of importance sampling, as shown by Annis et al. [2019].

This overlap is quantified by the KL divergence term in Eq. 32. Maintaining small KL divergences between adjacent power posteriors can be achieved by clustering temperatures in regions where $P(z | \mathbf{x}^{(b)}, \mathbf{f}, \Phi, t_k)$ changes rapidly. To accomplish this, we follow Calderhead and Girolami [2009] in adopting a power-law relationship to schedule the temperatures of Eq. 31:

$$t_k = \left(\frac{k}{N_t} \right)^p, \quad k = 0, 1, \dots, N_t,$$

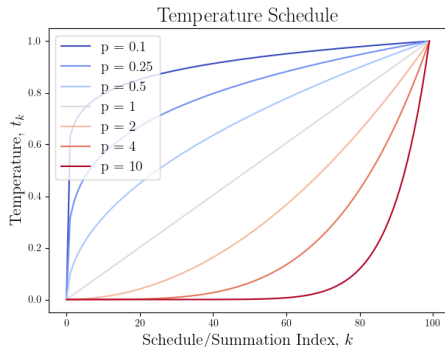


Figure 6: Power-law schedule.

The effect of varying p on the schedule between 0 and 1 is visualized in Fig. 6. When $p > 1$, spacing becomes denser near $t = 0$, while $p < 1$ creates denser spacing near $t = 1$. The impact of varying p on the discretized Thermodynamic Integral of Eq. 32 is illustrated in Fig. 5. The plots demonstrate that for $p > 1$, the trapezoidal bins are clustered closer to $t = 0$, concentrating the discrete approximation error towards $t = 1$.

The study by Calderhead and Girolami [2009] derives an analytic term for an optimal tempering distribution in the context of linear regression models, where the power posterior in Eq. 30 is used to evaluate the plausibility of model parameters in relation to the data, rather than reflecting a latent variable posterior. However, their findings may not hold in the context of T-KAM and generative modeling, making p and the temperature schedule difficult variables to tune.

Instead, we schedule p cyclically across all parameter updates of T-KAM’s training procedure, similar to the previous work of Fu et al. [2019]. The initial and final p ’s and the number of cycles are treated as tunable hyperparameters:

$$\delta = \text{linspace}(0, 2\pi(N_{\text{cycles}} + 0.5); \text{len} = N_{\text{updates}})$$

$$p(i) = p_{\text{init}} + \frac{p_{\text{end}} - p_{\text{init}}}{2} (1 - \cos \delta) \quad (38)$$

where N_{updates} denotes the total number of parameter updates, i indexes the current training iteration, N_{cycles} is the number of cycles, and δ is a vector of length N_{updates} .

Initializing $p > 1$ focuses learning on smoother likelihoods during the early stages of the cycle, where global features emerge between adjacent power posteriors. As training progresses, T-KAM will have learned the global features sufficiently well, reducing the change of measure between adjacent power posteriors of a $p > 1$ schedule. At this stage, $p(i)$ will have transitioned to $p \leq 1$, thereby shifting T-KAM’s focus towards capturing more detailed features of the posterior land-

scape, where training is expected to enhance its ability to generate finer details.

Guidance on selecting optimal values for the tempering hyperparameters is provided in Tab. 3.

4 Experiments

Gaussian Radial Basis Functions (RBF KANs), as presented by Li [2024], were used instead of the cubic B-spline bases proposed by Liu et al. [2024]. RBFs are more efficient for GPU implementation, and Poggio and Girosi [1990] previously demonstrated that radial functions provide an optimal solution to the regularized approximation/interpolation problem.

Fourier bases, (FFTs by Xu et al. [2024]), were also considered in Secs. 4.1 and 4.2, and Chebyshev bases, (Chebyshev by SS et al. [2024]), were considered in Sec. 4.3. However, FFTs were found to be non-smooth and potentially discontinuous, as illustrated by the prior distributions plotted in Sec. A.9. This may have compromised adherence to KART and future work might explore incorporating regularization to improve their smoothness.

To quantify the fidelity of generated data in a more reliable manner than previous studies in the literature, we used effectively unbiased metrics based on the principles outlined by Chong and Forsyth [2020]. By applying linear regression to extrapolate the values of standard metrics to an infinitely sized sample set, Monte Carlo error was mitigated, (otherwise associated with finite sample sizes).

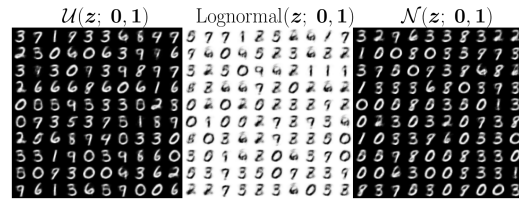
For Sec. 4.3, we gathered $\overline{\text{FID}}_\infty$ and $\overline{\text{KID}}_\infty$, which are effectively unbiased estimators of the Fréchet Inception Distance and Kernel Inception Distance, introduced by Heusel et al. [2018] and Bińkowski et al. [2021] respectively. The set of sample sizes used for the linear regression were: 1000, 1200, 1400, 1600, 1800, 2000, 2200, 2400, 2600, 2800, 3000.

However, we recognise that quantifying the fidelity of generated data is inherently challenging and not an exact science. While the metrics used in this study have limitations, they align with those commonly found in the literature. Our conclusions are also informed by our subjective perception of the images. Furthermore, no metrics were applied in Secs. 4.1 & 4.2, as vision metrics rely on the Inception V3 model trained on ImageNet (Szegedy et al. [2015]), potentially introducing bias against other datasets.

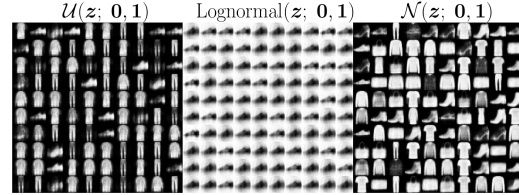
More image samples are provided in Sec. A.8.

4.1 MNIST & FMNIST with MLE / IS and adherence to KART

The MNIST and FMNIST datasets, introduced by Deng [2012] and Xiao et al. [2017] respectively, are grayscale datasets that can be modeled with the first likelihood model from Eq. 20. The first collection of benchmarks presented in Sec. A.2 were obtained using the hyperparameters and architecture specified for this experiment in Tab. 4. T-KAM was trained for 10 epochs with 20,000 training examples, an importance sample size of $N_s = 100$, and a batch size of $N_x = 100$, (corresponding to 2,000 parameter updates).



(a) MNIST



(b) FMNIST

Figure 7: Generated NIST images using three different exponentially-tilted priors, initialized from $\mathcal{N}(z; \mathbf{0}, \mathbf{1})$, $\text{Lognormal}(z; \mathbf{0}, \mathbf{1})$, and $\mathcal{U}(z; \mathbf{0}, \mathbf{1})$. Lognormal is inverted for clarity.

Lognormal priors introduced skew, leading to posterior mode collapse. T-KAM learned to generate an average of all MNIST or FMNIST classes, and failed to learn a meaningful latent prior. In contrast, Gaussian priors produced the sharpest images for FMNIST, and uniform priors yielded the sharpest MNIST digits.

4.2 2D Darcy flow pressures with MLE / IS and adherence to KART

The dataset used in this experiment was sourced from Li et al. [2021]. The Darcy flow equation is a second-order elliptic partial differential equation (PDE) that models various physical phenomena, including fluid flow through porous media and heat conduction. At steady state, its two-dimensional form on the unit square with Dirich-

let boundary conditions is given by:

$$\begin{aligned} -\nabla \cdot (k(\mathbf{z}), \nabla u(\mathbf{z})) &= f(\mathbf{z}), & \mathbf{z} \in [0, 1]^2, \\ u(\mathbf{z}) &= 0, & \mathbf{z} \in \partial[0, 1]^2, \end{aligned} \quad (39)$$

where $k(\mathbf{z})$ is the 2D permeability field, $u(\mathbf{z})$ represents the 2D pressure field, and $f(\mathbf{z})$ is a forcing function evaluated at \mathbf{z} .

Generating new flow-pressure samples is a challenging task in machine learning. One approach is to use input permeability samples while employing the Fourier Neural Operator (FNO), (presented by Li et al. [2021]), to learn the solution operator mapping between permeability and flow pressure. However, in this study, we use the purely generative task to illustrate how weak inductive biases can influence what T-KAM learns.

T-KAM was trained to generate new Darcy flow pressures using a batch size and importance sample size of $N_x = 50, N_s = 50$. The training spanned 600 epochs with 1,000 training examples, resulting in 12,000 parameter updates. All other hyperparameters are provided in Tab. 5.

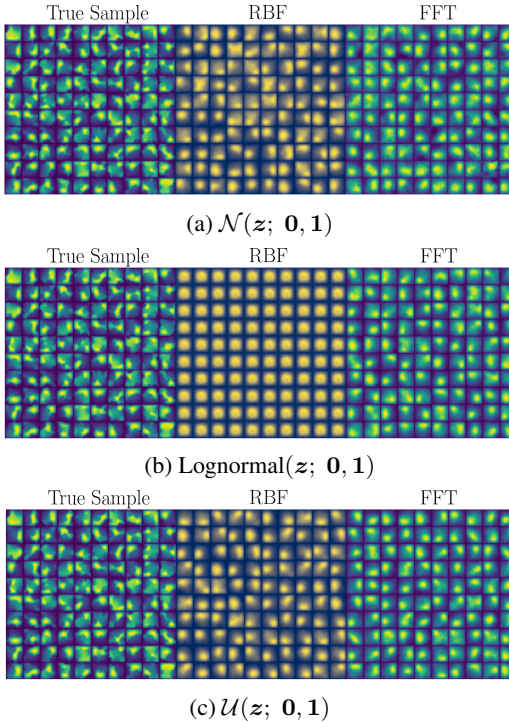


Figure 8: Generated Darcy flow pressures with exponentially-tilted priors initialized from standard Gaussian, lognormal, and uniform distributions. Radial Basis Functions, (RBFs by Li [2024]), are contrasted against Fourier bases, (FFTs by Xu et al. [2024]). RBF is colored differently for clarity.

While RBF bases led to oversmoothing, FFTs better captured large-scale variations. However, all priors produced similar generations, despite constraining different latent representations, plotted in Sec. A.9.

4.3 CIFAR-10 & SVHN with convolutional neural network and scaling strategies

T-KAM, when formulated with KART, can be interpreted as a dense or spline-based network. However, for spatial data, convolutional neural networks (CNNs), introduced by LeCun et al. [2015], are more suitable. In addition to their computational efficiency through weight sharing, CNNs offer a key advantage over dense networks due to their spatial inductive bias: sequences of convolutional layers implement shift-equivariant transformations that are well-suited for images.

T-KAM can be adapted to image generation by moving away from KART, and implementing the generator as a CNN.

To verify that T-KAM exhibits behaviour comparable to the model proposed by Pang et al. [2020] under similar posterior sampling strategies, we trained T-KAM on the CIFAR-10 and SVHN datasets, (introduced by Krizhevsky [2009] and Netzer et al. [2011], respectively), using a KAN prior and the CNN-based generator adopted in their approach.

This allowed us to compare the mixture prior with ITS against the deep prior with ULA (i.e., the approach of Pang et al. [2020]), and to assess whether SE can outperform MLE.

Due to limited computational resources during this study, (detailed in Sec. A.2), training was shortened from 70,000 to 8,000 parameter updates. Due to their parameter efficiency, Chebyshev bases were used for the prior, as introduced by SS et al. [2024]. The overall architecture mirrored that of Pang et al. [2020], though it is important to note that dense KANs do not directly replicate the behaviour of standard dense layers. Additionally, we used a single optimizer to train both models, rather than using separate optimizers for the prior and generator networks. We considered these discrepancies to be acceptable, given the comparative nature of this experiment.

We compared the following two approaches for scaling the prior:

1. the mixture distribution in Eq. 12, which uses ITS to generate samples from the prior
2. the deep prior in Eq. 14, which requires ULA for sampling from the prior.

Posterior sampling was conducted with ULA, and a Gaussian reference was used, $\pi_0 = \mathcal{N}(z; \mathbf{0}, \mathbf{1})$. SE and Parallel Tempering were also evaluated to verify their potential as a training strategy.

T-KAM was trained for 20 epochs with a batch size of $N_x = 100$ on 40,000 training examples. All remaining hyperparameters are provided in Tab. 6, and architectural details for the mixture and deep prior models, as well as the CNN generators, are included in Sec. A.5.1.

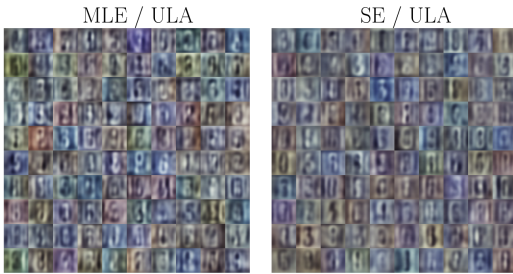
For brevity, only the SVHN images are visualized in the main body. Samples of CIFAR-10 are provided under Sec. A.8.5

Table 1: Effectively unbiased FID and KID scores (lower is better) for SVHN.

Prior	MLE	SE
Mixture	$\overline{\text{FID}}_\infty = 81.02$	$\overline{\text{FID}}_\infty = 82.13$
	$\overline{\text{KID}}_\infty = 0.0669$	$\overline{\text{KID}}_\infty = 0.0673$
Deep	$\overline{\text{FID}}_\infty = 107.42$	$\overline{\text{FID}}_\infty = 141.24$
	$\overline{\text{KID}}_\infty = 0.0970$	$\overline{\text{KID}}_\infty = 0.1320$

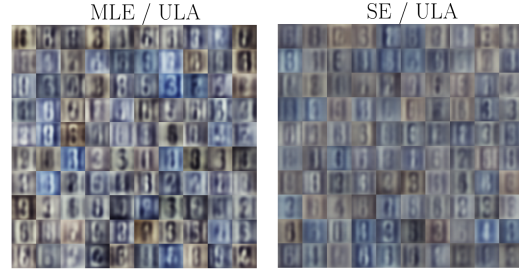
Table 2: Effectively unbiased FID and KID scores (lower is better) for CIFAR-10.

Prior	MLE	SE
Mixture	$\overline{\text{FID}}_\infty = 159.11$	$\overline{\text{FID}}_\infty = 180.00$
	$\overline{\text{KID}}_\infty = 0.1600$	$\overline{\text{KID}}_\infty = 0.1858$
Deep	$\overline{\text{FID}}_\infty = 185.10$	$\overline{\text{FID}}_\infty = 201.75$
	$\overline{\text{KID}}_\infty = 0.1780$	$\overline{\text{KID}}_\infty = 0.1977$



(a) SVHN with mixture prior and MLE (b) SVHN with mixture prior and SE

Figure 9: Generated samples from T-KAM trained on SVHN using a mixture prior.



(a) SVHN with deep prior and MLE (b) SVHN with deep prior and SE

Figure 10: Generated samples from T-KAM trained on SVHN using a deep prior.

The mixture prior with ITS outperformed the deep prior with ULA, while also being more computationally efficient and enabling faster inference. This advantage is likely due to ITS providing exact samples from the prior, whereas ULA produces only approximate, biased samples.

SE did not outperform MLE and cannot be justified in this setting given its computational overhead. Alternative approaches, such as different annealing schedules or the use of autoMALA with bias correction and temperature-adaptive step size tuning, could improve performance, but they are not worth the added complexity, hyperparameter tuning, and extended training time.

5 Future work

5.1 Hardware acceleration

Computational benchmarks are provided in Sec. A.2. The univariate and localized nature of spline interpolations complicates their parallelization on GPUs, as noted by Yang and Wang [2024]. Additionally, the search operations in Eqs. 13, 24, and 77 were parallelized on the CPU across samples, even though the remainder of T-KAM was executed on the GPU. This design choice stems from the fact that GPUs are generally ill-suited for parallelized search algorithms, which often rely on conditional logic. Parallelizing conditionals can lead to thread divergence, making CPUs more efficient for these operations.

While ITS enables fast inference and scales when the prior is a mixture model, T-KAM’s training with ULA does not scale efficiently on GPUs due to the iterative, gradient-based nature of ULA.

Nonetheless, the unique advantages of T-KAM justify continued research and development. Notably, Zetta [2024] introduces the Learnable Function Unit (LFU), a processor designed for efficient evaluation and differentiation of univariate, non-

linear functions in parallel, while offering precise data flow control and high throughput.

The LFU presents a promising avenue for more efficient implementations of ULA, and improved posterior sampling, potentially including bias correction and adaptive step size tuning with autoMALA, (Sec. A.7.5). Even without annealing, replacing ULA with autoMALA may yield a more robust probabilistic model with stronger theoretical guarantees.

Overall, T-KAM may prove more scalable than conventional generative models, owing to its reliance on finite representations of continuous functions and its compatibility with the LFU.

5.2 Text-to-text, classification, and multi-modal generation

Pang and Wu [2021] provided a robust framework for high-quality text-to-text generation, classification, and semi-supervised learning, while Yuan et al. [2024] demonstrated how T-KAM might be adapted into a multi-modal generative model. This holds promise for future investigations and industry adoption, especially when the hardware of Zetta [2024] becomes available. However, the symbol-vector coupling approach of Pang and Wu [2021] must first be adapted to remain compatible with ITS.

5.3 Improved sampling for multimodal distributions

Despite its theoretical guarantees, annealing is difficult to justify given its computational cost and limited practical benefit. Future work could explore adaptations of the hierarchical EBMs proposed by Cui and Han [2024], without sacrificing the interpretability or efficiency of our model.

References

Jeffrey Annis, Nathan J. Evans, Brent J. Miller, and Thomas J. Palmeri. Thermodynamic integration and steppingstone sampling methods for estimating bayes factors: A tutorial. *Journal of Mathematical Psychology*, 89:67–86, April 2019. doi: 10.1016/j.jmp.2019.01.005. URL <https://osf.io/jpn4>. Epub 2019 Feb 13.

Leonard Bereska and Efstratios Gavves. Mechanistic interpretability for ai safety – a review, 2024. URL <https://arxiv.org/abs/2404.14082>.

Mikołaj Bińkowski, Danica J. Sutherland, Michael Arbel, and Arthur Gretton. Demystifying mmd gans, 2021.

Miguel Biron-Lattes, Nikola Surjanovic, Saifuddin Syed, Trevor Campbell, and Alexandre Bouchard-

Côté. automala: Locally adaptive metropolis-adjusted langevin algorithm, 2024. URL <https://arxiv.org/abs/2310.16782>.

Pakshal Bohra, Joaquim Campos, Harshit Gupta, Shayan Aziznejad, and Michael Unser. Learning activation functions in deep (spline) neural networks. *IEEE Open Journal of Signal Processing*, 1:295–309, 2020. doi: 10.1109/OJSP.2020.3039379.

Zavareh Bozorgasl and Hao Chen. Wav-kan: Wavelet kolmogorov-arnold networks, 2024. URL <https://arxiv.org/abs/2405.12832>.

Steve Brooks, Andrew Gelman, Galin Jones, and Xiao-Li Meng. *Handbook of Markov Chain Monte Carlo*. Chapman and Hall/CRC, May 2011. ISBN 9780429138508. doi: 10.1201/b10905. URL <http://dx.doi.org/10.1201/b10905>.

Ben Calderhead and Mark Girolami. Estimating bayes factors via thermodynamic integration and population mcmc. *Computational Statistics & Data Analysis*, 53(12):4028–4045, 2009. ISSN 0167-9473. doi: <https://doi.org/10.1016/j.csda.2009.07.025>. URL <https://www.sciencedirect.com/science/article/pii/S0167947309002722>.

Min Jin Chong and David Forsyth. Effectively unbiased fid and inception score and where to find them, 2020.

Jiali Cui and Tian Han. Learning latent space hierarchical ebm diffusion models, 2024. URL <https://arxiv.org/abs/2405.13910>.

Li Deng. The mnist database of handwritten digit images for machine learning research. *IEEE Signal Processing Magazine*, 29(6):141–142, 2012.

Luc Devroye. Chapter 4 nonuniform random variate generation. In Shane G. Henderson and Barry L. Nelson, editors, *Simulation*, volume 13 of *Handbooks in Operations Research and Management Science*, pages 83–121. Elsevier, 2006. doi: [https://doi.org/10.1016/S0927-0507\(06\)13004-2](https://doi.org/10.1016/S0927-0507(06)13004-2). URL <https://www.sciencedirect.com/science/article/pii/S0927050706130042>.

Randal Douc, Olivier Cappé, and Eric Moulines. Comparison of resampling schemes for particle filtering, 2005. URL <https://arxiv.org/abs/cs/0507025>.

Simon Duane, A.D. Kennedy, Brian J. Pendleton, and Duncan Roweth. Hybrid monte carlo. *Physics Letters B*, 195(2):216–222, 1987. ISSN 0370-2693. doi: [https://doi.org/10.1016/0370-2693\(87\)91197-X](https://doi.org/10.1016/0370-2693(87)91197-X). URL <https://www.sciencedirect.com/science/article/pii/037026938791197X>.

S. Dzhenezher and A. Skopenkov. A structured proof of kolmogorov’s superposition theorem, 2022. URL <https://arxiv.org/abs/2105.00408>.

- N. Friel and A. N. Pettitt. Marginal likelihood estimation via power posteriors. *Journal of the Royal Statistical Society. Series B (Statistical Methodology)*, 70(3):589–607, 2008. ISSN 13697412, 14679868. URL <http://www.jstor.org/stable/20203843>.
- Hao Fu, Chunyuan Li, Xiaodong Liu, Jianfeng Gao, Asli Celikyilmaz, and Lawrence Carin. Cyclical annealing schedule: A simple approach to mitigating kl vanishing, 2019. URL <https://arxiv.org/abs/1903.10145>.
- Alexander B. Givental, Boris A. Khesin, Jerrold E. Marsden, Alexander N. Varchenko, Victor A. Vasiliev, Oleg Ya. Viro, and Vladimir M. Zakalyukin, editors. *On the representation of functions of several variables as a superposition of functions of a smaller number of variables*, pages 25–46. Springer Berlin Heidelberg, Berlin, Heidelberg, 2009. ISBN 978-3-642-01742-1. doi: 10.1007/978-3-642-01742-1_5. URL https://doi.org/10.1007/978-3-642-01742-1_5.
- W. K. Hastings. Monte carlo sampling methods using markov chains and their applications. *Biometrika*, 57(1):97–109, 04 1970. ISSN 0006-3444. doi: 10.1093/biomet/57.1.97. URL <https://doi.org/10.1093/biomet/57.1.97>.
- Martin Heusel, Hubert Ramsauer, Thomas Unterthiner, Bernhard Nessler, and Sepp Hochreiter. Gans trained by a two time-scale update rule converge to a local nash equilibrium, 2018.
- Koji Hukushima and Koji Nemoto. Exchange monte carlo method and application to spin glass simulations. *Journal of the Physical Society of Japan*, 65(6):1604–1608, June 1996. ISSN 1347-4073. doi: 10.1143/jpsj.65.1604. URL <http://dx.doi.org/10.1143/JPSJ.65.1604>.
- JuliaCI. Benchmarktools.jl, 2024. URL <https://juliaci.github.io/BenchmarkTools.jl/stable/>. Accessed on August 20, 2024.
- Jared Kaplan, Sam McCandlish, Tom Henighan, Tom B. Brown, Benjamin Chess, Rewon Child, Scott Gray, Alec Radford, Jeffrey Wu, and Dario Amodei. Scaling laws for neural language models, 2020. URL <https://arxiv.org/abs/2001.08361>.
- Diederik P. Kingma and Max Welling. Auto-encoding variational bayes, 2022. URL <https://arxiv.org/abs/1312.6114>. arXiv:1312.6114.
- T. Kloek and H. K. van Dijk. Bayesian estimates of equation system parameters: An application of integration by monte carlo. *Econometrica*, 46(1): 1–19, 1978. ISSN 00129682, 14680262. URL <http://www.jstor.org/stable/1913641>.
- Alex Krizhevsky. Learning multiple layers of features from tiny images. pages 32–33, 2009. URL <https://www.cs.toronto.edu/~kriz/learning-features-2009-TR.pdf>.
- R. Larson and B.H. Edwards. *Calculus of a Single Variable*. Cengage Learning, 2008. ISBN 9780547209982. URL https://books.google.co.uk/books?id=gr7nGg5_9xcC.
- Dirk Laurie. Calculation of gauss-kronrod quadrature rules. *Math. Comput.*, 66:1133–1145, 07 1997. doi: 10.1090/S0025-5718-97-00861-2.
- Yann LeCun, Yoshua Bengio, and Geoffrey Hinton. Deep learning. *Nature*, 521(7553):436–444, May 28 2015. ISSN 1476-4687. doi: 10.1038/nature14539.
- Ziyao Li. Kolmogorov-arnold networks are radial basis function networks, 2024. URL <https://arxiv.org/abs/2405.06721>.
- Zongyi Li, Nikola Kovachki, Kamyar Azizzadenesheli, Burigede Liu, Kaushik Bhattacharya, Andrew Stuart, and Anima Anandkumar. Fourier neural operator for parametric partial differential equations, 2021. URL <https://arxiv.org/abs/2010.08895>.
- Ziming Liu, Yixuan Wang, Sachin Vaidya, Fabian Ruehle, James Halverson, Marin Soljačić, Thomas Y. Hou, and Max Tegmark. Kolmogorov-arnold networks, 2024. URL <https://arxiv.org/abs/2404.19756>.
- E. Marinari and G. Parisi. Simulated tempering: A new monte carlo scheme. *Europhysics Letters*, 19(6):451, jul 1992. doi: 10.1209/0295-5075/19/6/002. URL <https://dx.doi.org/10.1209/0295-5075/19/6/002>.
- Nicholas Metropolis and S. Ulam. The monte carlo method. *Journal of the American Statistical Association*, 44(247):335–341, 1949. ISSN 01621459, 1537274X. URL <http://www.jstor.org/stable/2280232>.
- Radford M. Neal. Annealed importance sampling, 1998. URL <https://arxiv.org/abs/physics/9803008>.
- Yuval Netzer, Tao Wang, Adam Coates, Alessandro Bissacco, Bo Wu, and Andrew Y. Ng. Reading digits in natural images with unsupervised feature learning. In *NIPS Workshop on Deep Learning and Unsupervised Feature Learning 2011*, 2011. URL http://ufldl.stanford.edu/housenumbers/nips2011_housenumbers.pdf.
- Erik Nijkamp, Mitch Hill, Tian Han, Song-Chun Zhu, and Ying Nian Wu. On the anatomy of mcmc-based maximum likelihood learning of energy-based models, 2019a. URL <https://arxiv.org/abs/1903.12370>.
- Erik Nijkamp, Mitch Hill, Song-Chun Zhu, and Ying Nian Wu. Learning non-convergent non-persistent short-run mcmc toward energy-based model, 2019b. URL <https://arxiv.org/abs/1904.09770>.

- Bo Pang and Ying Nian Wu. Latent space energy-based model of symbol-vector coupling for text generation and classification, 2021. URL <https://arxiv.org/abs/2108.11556>.
- Bo Pang, Tian Han, Erik Nijkamp, Song-Chun Zhu, and Ying Nian Wu. Learning latent space energy-based prior model, 2020. URL <https://arxiv.org/abs/2006.08205>.
- T. Poggio and F. Girosi. Networks for approximation and learning. *Proceedings of the IEEE*, 78(9): 1481–1497, 1990. doi: 10.1109/5.58326. URL <https://doi.org/10.1109/5.58326>.
- Maziar Raissi, Alireza Yazdani, and George Em Karniadakis. Hidden fluid mechanics: A navier-stokes informed deep learning framework for assimilating flow visualization data, 2018. URL <https://arxiv.org/abs/1808.04327>.
- G. O. Roberts and O. Stramer. Langevin diffusions and metropolis-hastings algorithms. *Methodology and Computing in Applied Probability*, 4(4): 337–357, 2002. ISSN 1573-7713. doi: 10.1023/A:1023562417138. URL <https://doi.org/10.1023/A:1023562417138>.
- P. J. Rossky, J. D. Doll, and H. L. Friedman. Brownian dynamics as smart monte carlo simulation. *The Journal of Chemical Physics*, 69(10):4628–4633, 11 1978. ISSN 0021-9606. doi: 10.1063/1.436415. URL <https://doi.org/10.1063/1.436415>.
- Sidharth SS, Keerthana AR, Gokul R, and Anas KP. Chebyshev polynomial-based kolmogorov-arnold networks: An efficient architecture for nonlinear function approximation, 2024. URL <https://arxiv.org/abs/2405.07200>.
- Robert Swendsen and Jian-Sheng Wang. Replica monte carlo simulation of spin-glasses. *Physical review letters*, 57:2607–2609, 12 1986. doi: 10.1103/PhysRevLett.57.2607.
- Christian Szegedy, Vincent Vanhoucke, Sergey Ioffe, Jonathon Shlens, and Zbigniew Wojna. Rethinking the inception architecture for computer vision, 2015.
- Carole-Jean Wu, Ramya Raghavendra, Udit Gupta, Bilge Acun, Newsha Ardalani, Kiwan Maeng, Gloria Chang, Fiona Aga Behram, James Huang, Charles Bai, Michael Gschwind, Anurag Gupta, Myle Ott, Anastasia Melnikov, Salvatore Candido, David Brooks, Geeta Chauhan, Benjamin Lee, Hsien-Hsin S. Lee, Bugra Akyildiz, Maximilian Balandat, Joe Spisak, Ravi Jain, Mike Rabbat, and Kim Hazelwood. Sustainable ai: Environmental implications, challenges and opportunities, 2022. URL <https://arxiv.org/abs/2111.00364>.
- Han Xiao, Kashif Rasul, and Roland Vollgraf. Fashion-mnist: a novel image dataset for benchmarking machine learning algorithms, 2017. URL <https://arxiv.org/abs/1708.07747>.
- Jinfeng Xu, Zheyu Chen, Jinze Li, Shuo Yang, Wei Wang, Xiping Hu, and Edith C. H. Ngai. Fourierkangcf: Fourier kolmogorov-arnold network – an effective and efficient feature transformation for graph collaborative filtering, 2024. URL <https://arxiv.org/abs/2406.01034>.
- Xingyi Yang and Xinchao Wang. Kolmogorov-arnold transformer, 2024. URL <https://arxiv.org/abs/2409.10594>.
- Shiyu Yuan, Jiali Cui, Hanao Li, and Tian Han. Learning multimodal latent generative models with energy-based prior, 2024. URL <https://arxiv.org/abs/2409.19862>.
- Zetta. Zetta, the next paradigm of sustainable computing. <https://zettalaboratories.com/litepaper>, August 2024. Zetta introduces a polymorphic computing chip technology, achieving up to 27.6x efficiency gains over the H100 GPUs through dynamically reconfigurable hardware that adapts to diverse AI models via software configuration.
- Xinwei Zhang, Zhiqiang Tan, and Zhijian Ou. Persistently trained, diffusion-assisted energy-based models, 2023. URL <https://arxiv.org/abs/2304.10707>.
- Song Chun Zhu and D. Mumford. Grade: Gibbs reaction and diffusion equations. In *Sixth International Conference on Computer Vision (IEEE Cat. No.98CH36271)*, pages 847–854, 1998. doi: 10.1109/ICCV.1998.710816.

A Appendix

A.1 Codebase

The study was implemented in Julia at <https://github.com/exa-laboratories/T-KAM>.

A.2 Computational benchmarks

The following benchmarks were collected for FP32 on a GPU (NVIDIA GeForce GTX 1650) with Julia’s BenchmarkTools package, provided by JuliaCI [2024]. The index search operations in Eqs. 24, 13, & 77 were parallelized across 20 threads on a CPU (i7-9750H @ 2.60GHz). They reflect the computational cost of initializing T-KAM and performing a single reverse autodifferentiation of its loss functions, (Eqs. 16 and 34).

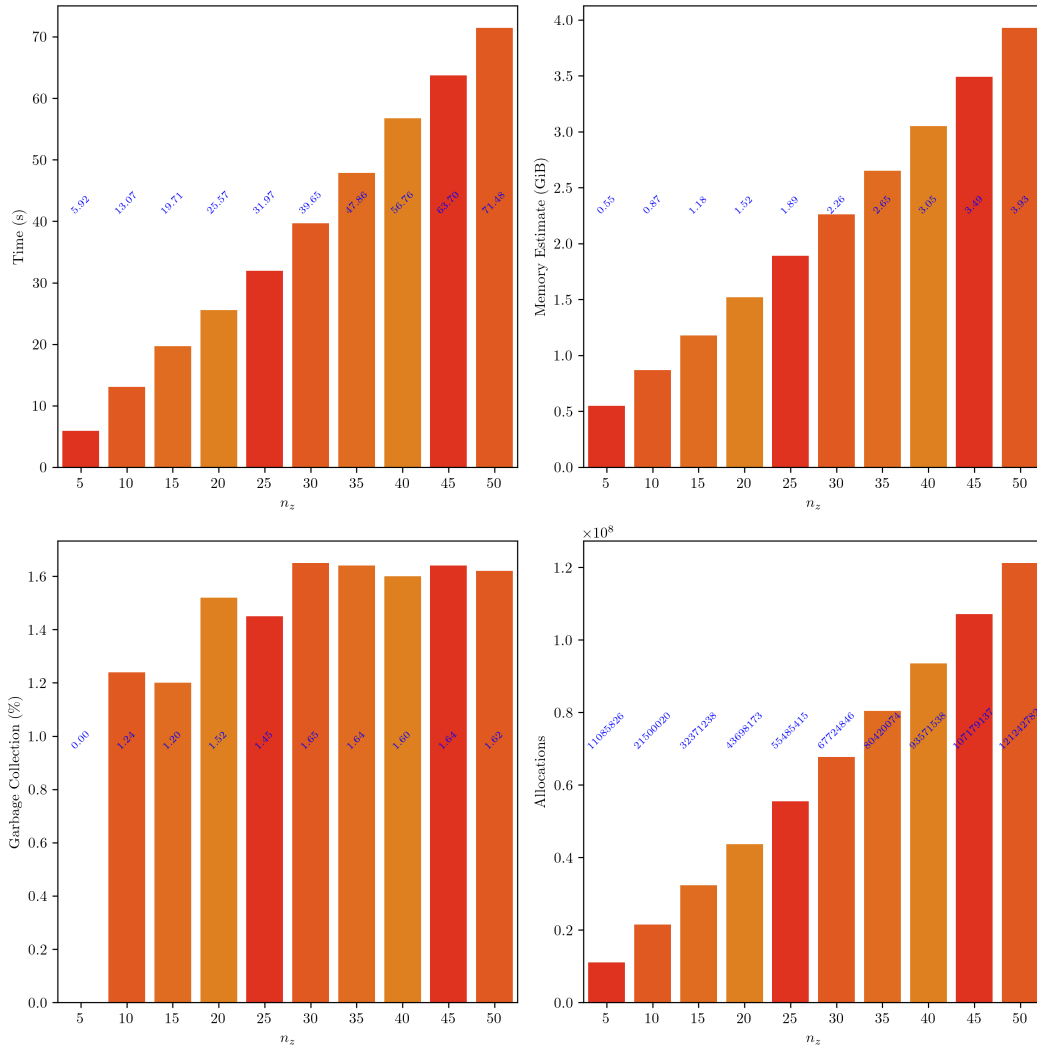


Figure 11: Computational benchmarks for varying latent dimensions, n_z , while adhering to KART with MLE / IS. The latent prior had an input size of n_z and an output size of $2n_z + 1$. The generator received inputs of size $2n_z + 1$, with a hidden size of $4n_z + 2$ and an output size of 28×28 . All other hyperparameters were kept consistent with Tab. 4.

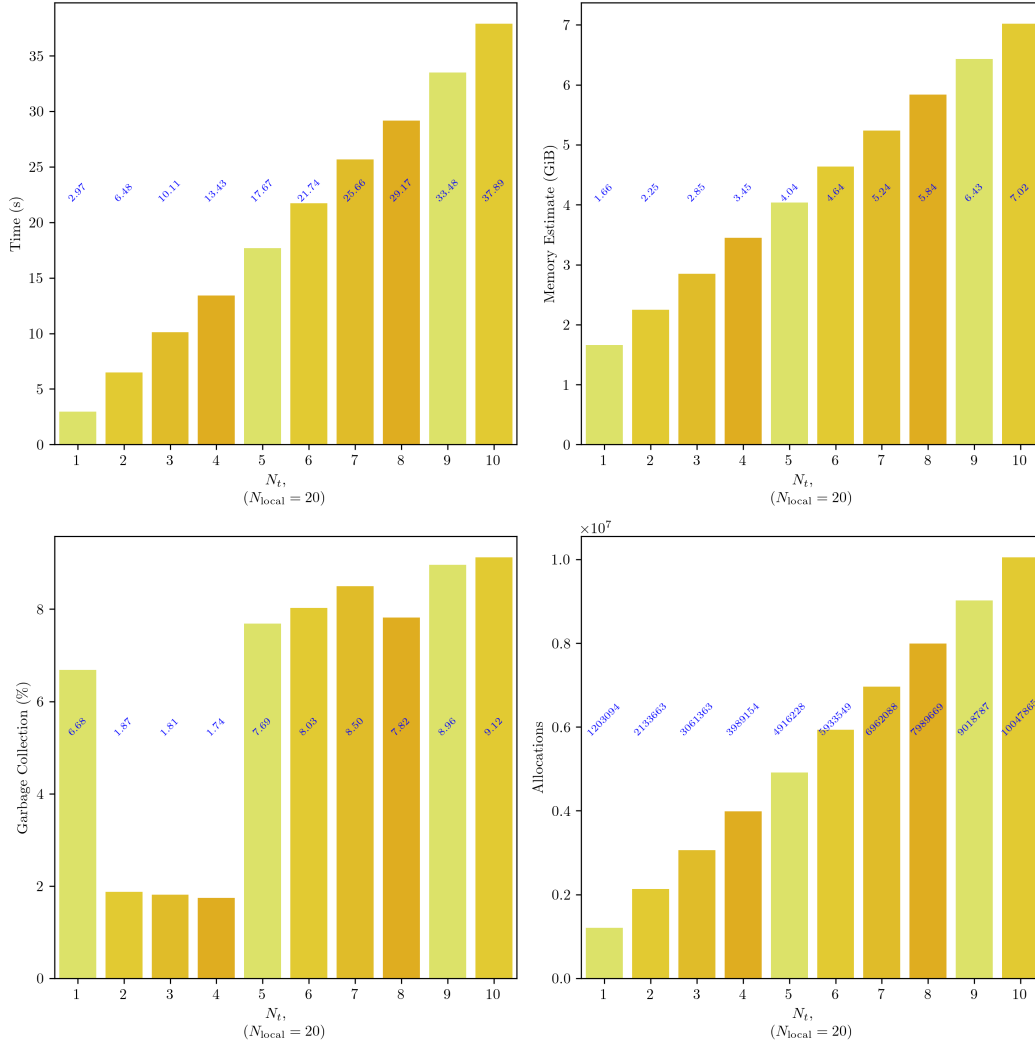


Figure 12: Computational benchmarks for varying amounts of ULA steps, N_t , while adhering to KART with SE / ULA. All other hyperparameters were kept consistent with Tab. 4 using the mixture univariate prior model.

A.3 Sustainability

Wu et al. [2022] showed that scaling outpaces advances in system hardware, and that seemingly promising approaches to sustainable scaling, such as training large, sparsely-activated neural networks or using data centers powered by carbon-free energy, fall short as realistic solutions. They also highlighted that the share of energy footprint to support Meta’s RM1 (language model) followed a 31:29:40 ratio in 2021, dedicated to data processing, experimentation/training, and inference, respectively. This insight guides our prioritization of fast inference over training:

1. Experimentation:

- T-KAM is expected to require less hyperparameter optimization, as layer configurations can be determined by KART.
- Given T-KAM’s function-based interpretability, we claim that task knowledge can often inform hyperparameters for the bases used in KANs.

2. Training:

- Three training approaches are proposed in this study. The first approach, MLE / IS, is efficient and can be applied when prior-posterior alignment is facilitated by existing task knowledge before training.
- The second approach, MLE / ULA, relies on short-run, unadjusted MCMC to maintain computational efficiency during training.
- Once trained, latent priors can be visualized and recovered, potentially providing insight into the latent space and facilitating transfer learning to reduce training time. Otherwise, a trained prior model can also be extracted and used to train another generator model.

3. Inference:

- Fast yet high-quality inference is facilitated in the baseline model by its use of inverse transform sampling (ITS) from the latent prior, made feasible due to the continuity-preserving, univariate, and finite-domain nature of the prior’s components. This is scalable when using the mixture model in Eq. 12 to facilitate inter-dimensional prior relationships.
- Both MLE / ULA and SE / ULA can be conducted with unadjusted Langevin sampling from a deepened prior to ensure that inference speed is always preserved post-training. Parallel Tempering is only used for posterior sampling during training.
- Training with regularization for both the prior and generator enables pruning or size reduction, following the scheme proposed by Liu et al. [2024] for KANs. This allows further compression beyond the baseline structure defined by KART.

A.4 Guidance on tempering hyperparameters

Table 3: Tempering hyperparameters.

Hyperparameter	Description
$N_t > 1$	Specifies the number of power posteriors, enabling a smooth transition between the prior and posterior. Increasing this improves exploration but also increases cost due to the need for more MALA iterations. Typically, this is limited and therefore guided by hardware availability, such as $N_t = 5$.
$N_{\text{local}} > 1$	Determines the number of ULA or autoMALA iterations per power posterior. Although increasing this value improves the quality of samples at each stage, it also raises the computational cost, much like N_t . It can be kept at a moderate value, such as $N_{\text{local}} = 20$, (based on the recommendations of Nijkamp et al. [2019b] and Nijkamp et al. [2019a] regarding short-run Markov chain Monte Carlo).
$N_{\text{unadjusted}} > 1$	Controls the number of autoMALA iterations performed without MH adjustments, reflecting the level of exploration at each power posterior. This can be set to 1, as guided by Biron-Lattes et al. [2024].
$p_{\text{init}} > 1, p_{\text{end}} \leq 1, N_{\text{cycles}}$	Controls the evolution of tempering during training. If the data is expected to have smooth relationships, reduce both p_{init} and p_{end} . For data with finer details, increase both values to allow for better focus on capturing intricate features. Recommended values are $p_{\text{init}} = 4$, and $p_{\text{end}} = 1$, since our experience suggests that power posteriors change rapidly closer to the prior.

A.5 Hyperparameters and training details

Table 4: Hyperparameters for Sec. 4.1.

EBM Prior		
layer_widths	p, q	40, 81
spline_type	(-)	variable
spline_activation	(-)	Silu
layer_norm	(-)	true
quadrature_method	(-)	gausslegendre
spline_degree	d	3
grid_size	N_{grid}	RBF: 20 FFT: 50
grid_update_ratio	α_{grid}	0.05
grid_range	$[z_{\min}, z_{\max}]$	Uniform: $[0, 1]$ Lognormal: $[0, 4]$ Gaussian: $[-1.2, 1.2]$
Spline basis ε init.	ε	0.1
Spline basis μ scaling	μ	1.0
Basis activation scaling	σ_b	1.0
Basis spline scaling	σ_s	1.0
Initial basis param.	τ_0	1.0
Train basis param.	$\tau_{\text{trainable}}$	true
GaussQuad_nodes	N_{quad}	100
Use mixture prior	(-)	false
KAN Likelihood		
hidden_widths	$q, 2q + 1$	81, 162
All other KAN hparams	Identical to EBM Prior	
generator_variance	σ_ϵ	1.0
output_activation	σ_{act}	sigmoid
Importance sampling resampler	resampler	residual
ESS threshold	γ	0.5
Grid updating		
update_prior_grid	(-)	true
update_llhood_grid	(-)	true
num_grid Updating_samples	(-)	50
grid_update_frequency	(-)	100
grid_update_decay	(-)	0.999
Training		
batch_size	N_x	100
importance_sample_size	N_s	100
Training examples	N_{train}	20,000
Testing examples	N_{test}	100
num_generated_samples	(-)	3,000
Number of epochs	N_{epochs}	10
eps	ϵ	0.001
Optimizer		
type	(-)	adam
learning_rate	η_{LR}	0.001
betas	(-)	(0.9, 0.999)

Table 5: Hyperparameters for Sec. 4.2.

EBM Prior		
layer_widths	p, q	40, 81
spline_type	(-)	variable
spline_activation	(-)	Silu
layer_norm	(-)	true
quadrature_method	(-)	gausslegendre
spline_degree	d	3
grid_size	N_{grid}	RBF: 20 FFT: 50
grid_update_ratio	α_{grid}	0.05
grid_range	$[z_{\min}, z_{\max}]$	Uniform: $[0, 1]$ Lognormal: $[0, 4]$ Gaussian: $[-1.2, 1.2]$
Spline basis ε init.	ε	0.1
Spline basis μ scaling	μ	1.0
Basis activation scaling	σ_b	1.0
Basis spline scaling	σ_s	1.0
Initial basis param.	τ_0	1.0
Train basis param.	$\tau_{\text{trainable}}$	true
GaussQuad_nodes	N_{quad}	100
Use mixture prior	(-)	false
KAN Likelihood		
hidden_widths	$q, 2q + 1$	81, 162
All other KAN hparams	Identical to EBM Prior	
generator_variance	σ_ϵ	0.1
output_activation	σ_{act}	sigmoid
Importance sampling resampler	resampler	residual
ESS threshold	γ	0.5
Grid updating		
update_prior_grid	(-)	true
update_llhood_grid	(-)	true
num_grid Updating samples	(-)	100
grid_update_frequency	(-)	100
grid_update_decay	(-)	0.999
Training		
batch_size	N_x	50
importance_sample_size	N_s	50
Training examples	N_{train}	1,000
Testing examples	N_{test}	1,000
num_generated_samples	(-)	3,000
Number of epochs	N_{epochs}	600
eps	ϵ	0.001
Optimizer		
type	(-)	adam
learning_rate	η_{LR}	0.001
betas	(-)	(0.9, 0.999)

A.5.1 SVHN & CIFAR-10 Architectures

Table 7: Dense Chebyshev KAN architecture for mixture prior model

Layer	Operation	Output Dim.
Input	Latent vector z	$p = 100$
100	Dense(100)	$q = 201$

sizes=[100,201]

Table 6: Hyperparameters for Sec. 4.3.

EBM Prior		
layer_widths	p, q	See Sec. A.5.1
spline_type	(-)	Cheby
spline_activation	(-)	Silu
layer_norm	(-)	false
quadrature_method	(-)	gausslegendre
spline_degree	d	3
grid_size	N_{grid}	0, (Chebyshev requires no grid)
grid_update_ratio	α_{grid}	N/A
grid_range	$[z_{\text{min}}, z_{\text{max}}]$	$[-1.2, 1.2]$
Spline basis ε init.	ε	0.1
Spline basis μ scaling	μ	1.0
Basis activation scaling	σ_b	1.0
Basis spline scaling	σ_s	1.0
Initial basis param.	τ_0	1.01
Train basis param.	$\tau_{\text{trainable}}$	false
GaussQuad_nodes	N_{quad}	100
Use mixture prior	(-)	variable
KAN Likelihood		
cnn_widths	(-)	See Sec. A.5.1
All other KAN hparams		N/A
generator_variance	σ_ϵ	0.3
output_activation	σ_{act}	sigmoid
Importance sampling resampler	resampler	Not used
ESS threshold	γ	N/A
Grid updating		
update_prior_grid	(-)	false
update_llhood_grid	(-)	false
Training		
batch_size	N_x	100
importance_sample_size	N_s	N/A
Training examples	N_{train}	40,000
Testing examples	N_{test}	100
num_generated_samples	(-)	3,000
Number of epochs	N_{epochs}	20
eps	ϵ	0.0001
Optimizer		
type	(-)	adam
learning_rate	η_{LR}	0.0005
betas	(-)	(0.9, 0.999)
PRIOR_LANGEVIN		
iters	N_{local}	60
step_size	η	0.16
POSTERIOR_LANGEVIN		
iters	N_{local}	SVHN: 20 CIFAR10: 40
step_size	η	0.01
THERMODYNAMIC_INTEGRATION		
iters	N_{local}	20
num_temps	N_t	5
Initial exponent in power law schedule	p_{start}	4
Final exponent in power law schedule	p_{end}	1
num_cycles	N_{cycles}	0
Global swap frequency, replica_exchange_frequency	(-)	1

Table 8: Dense Chebyshev KAN architecture for deep prior model

Layer	Operation	Output Dim.
Input	Latent vector z	$p = 100$
100	Dense(100)	200
200	Dense(200)	200
200	Dense(200)	$q = 1$

sizes=[100,200,200,1]

Table 9: CNN Generator Architecture for SVHN

Layer	Operation	Output Shape	Stride
Input	Latent vector z reshaped	$1 \times 1 \times q$	–
1	4×4 convT(512), LeakyReLU	$4 \times 4 \times 512$	1
2	4×4 convT(256), LeakyReLU	$8 \times 8 \times 256$	2
3	4×4 convT(128), LeakyReLU	$16 \times 16 \times 128$	2
4	4×4 convT(3), Sigmoid	$32 \times 32 \times 3$	2

Config: kernel=4, strides=1/2/2/2, paddings=0/1/1/1, activation=LeakyReLU, batchnorm=False

Table 10: CNN Generator Architecture for CIFAR-10

Layer	Operation	Output Shape	Stride
Input	Latent vector z reshaped	$1 \times 1 \times q$	–
1	8×8 convT(1024), LeakyReLU	$8 \times 8 \times 1024$	1
2	4×4 convT(512), LeakyReLU	$16 \times 16 \times 512$	2
3	4×4 convT(256), LeakyReLU	$32 \times 32 \times 256$	2
4	3×3 convT(3), Sigmoid	$32 \times 32 \times 3$	1

Config: kernel=8/4/4/3, strides=1/2/2/1, paddings=0/1/1/1, activation=LeakyReLU, batchnorm=False

A.6 Derivations and other identities

A.6.1 Useful proof

The following short proof for a learning gradient with respect to an arbitrary set of parameters, θ , proves useful for other derivations in this study:

$$\begin{aligned}
 \mathbb{E}_{P(\mathbf{x}|\theta)} [\nabla_{\theta} \log P(\mathbf{x} | \theta)] &= \mathbb{E}_{P(\mathbf{x}|\theta)} \left[\frac{\nabla_{\theta} P(\mathbf{x} | \theta)}{P(\mathbf{x} | \theta)} \right] = \int_{\mathcal{X}} \frac{\nabla_{\theta} P(\mathbf{x} | \theta)}{P(\mathbf{x} | \theta)} dP(\mathbf{x} | \theta) \\
 &= \int_{\mathcal{X}} \nabla_{\theta} P(\mathbf{x} | \theta) d\mathbf{x} = \nabla_{\theta} \int_{\mathcal{X}} P(\mathbf{x} | \theta) d\mathbf{x} = \nabla_{\theta} 1 = 0. \quad (40)
 \end{aligned}$$

A.6.2 Marginal likelihood

$$\begin{aligned}
 \log \left(P(\mathbf{x}^{(b)} | \mathbf{f}, \Phi) \right) &= \mathbb{E}_{P(\mathbf{z}|\mathbf{x}^{(b)}, \mathbf{f}, \Phi)} \left[\log \left(P(\mathbf{x}^{(b)}, \mathbf{z} | \mathbf{f}, \Phi) \right) \right] \\
 &= \mathbb{E}_{P(\mathbf{z}|\mathbf{x}^{(b)}, \mathbf{f}, \Phi)} \left[\log \left(P(\mathbf{z} | \mathbf{f}) \cdot P(\mathbf{x}^{(b)} | \mathbf{z}, \Phi) \right) \right] \\
 &= \mathbb{E}_{P(\mathbf{z}|\mathbf{x}^{(b)}, \mathbf{f}, \Phi)} \left[\log(P(\mathbf{z} | \mathbf{f})) + \log \left(P(\mathbf{x}^{(b)} | \mathbf{z}, \Phi) \right) \right]. \quad (41)
 \end{aligned}$$

A.6.3 Maximum likelihood learning gradient

This proof demonstrates that the learning gradient with respect to an arbitrary set of parameters, θ , is independent of the sampling procedures in Sec. 2.6:

$$\begin{aligned}\mathbb{E}_{P(\mathbf{z}|\mathbf{x})} [\nabla_{\theta} \log P(\mathbf{x}, \mathbf{z})] &= \mathbb{E}_{P(\mathbf{z}|\mathbf{x})} [\nabla_{\theta} \log P(\mathbf{z} | \mathbf{x}) + \nabla_{\theta} \log P(\mathbf{x})] \\ &= \mathbb{E}_{P(\mathbf{z}|\mathbf{x})} [\nabla_{\theta} \log P(\mathbf{z} | \mathbf{x})] + \mathbb{E}_{P(\mathbf{z}|\mathbf{x})} [\nabla_{\theta} \log P(\mathbf{x})] \\ &= 0 + \nabla_{\theta} \log P(\mathbf{x}),\end{aligned}\tag{42}$$

where Eq. 40 has been used to zero the expected posterior. This allows gradient flow to be disregarded in the sampling procedures of Sec. 2.6 as shown in Eq. 16.

A.6.4 Contrastive divergence learning gradient for log-prior

The learning gradient attributed to the prior can be derived into a contrastive divergence framework, which is more typical of energy-based modeling literature. The prior model is solely dependent on \mathbf{f} in Eq. 4. We can rewrite Eq. 17 as:

$$\nabla_{\mathbf{f}} \log (P(\mathbf{z} | \mathbf{f})) = \nabla_{\mathbf{f}} \sum_{q=1}^{2n_z+1} \sum_{p=1}^{n_z} \log (\pi_{q,p}(z_{q,p})) = \nabla_{\mathbf{f}} \sum_{q=1}^{2n_z+1} \sum_{p=1}^{n_z} f_{q,p}(z_{q,p}) + \log (\pi_0(z_{q,p})) - \log (Z_{q,p})\tag{43}$$

where $Z_{q,p} = \int_{\mathcal{Z}} \exp(f_{q,p}(z_p)) d\pi_0(z_p)$ is the normalization constant. We can simplify the constant using Eq. 40:

$$\begin{aligned}\mathbb{E}_{P(\mathbf{z}|\mathbf{f})} \left[\nabla_{\mathbf{f}} \log P(\mathbf{z} | \mathbf{f}) \right] &= \mathbb{E}_{P(\mathbf{z}|\mathbf{f})} \left[\nabla_{\mathbf{f}} \sum_{q=1}^{2n_z+1} \sum_{p=1}^{n_z} f_{q,p}(z_{q,p}) + \log (\pi_0(z_{q,p})) - \log (Z_{q,p}) \right] = 0 \\ &= \mathbb{E}_{P(\mathbf{z}|\mathbf{f})} \left[\nabla_{\mathbf{f}} \sum_{q=1}^{2n_z+1} \sum_{p=1}^{n_z} f_{q,p}(z_{q,p}) \right] - \nabla_{\mathbf{f}} \sum_{q=1}^{2n_z+1} \sum_{p=1}^{n_z} \log (Z_{q,p}) = 0 \\ \therefore \nabla_{\mathbf{f}} \sum_{q=1}^{2n_z+1} \sum_{p=1}^{n_z} \log (Z_{q,p}) &= \mathbb{E}_{P(\mathbf{z}|\mathbf{f})} \left[\nabla_{\mathbf{f}} \sum_{q=1}^{2n_z+1} \sum_{p=1}^{n_z} f_{q,p}(z_{q,p}) \right]\end{aligned}\tag{44}$$

Therefore the log-prior gradient of Eq. 43 can be evaluated without quadrature normalization as:

$$\nabla_{\mathbf{f}} \log P(\mathbf{z} | \mathbf{f}) = \nabla_{\mathbf{f}} \sum_{q=1}^{2n_z+1} \sum_{p=1}^{n_z} f_{q,p}(z_{q,p}) - \mathbb{E}_{P(\mathbf{z}|\mathbf{f})} \left[\nabla_{\mathbf{f}} \sum_{q=1}^{2n_z+1} \sum_{p=1}^{n_z} f_{q,p}(z_{q,p}) \right],\tag{45}$$

and the learning gradient attributed to the prior is finalized into a contrastive divergence format:

$$\begin{aligned}\mathbb{E}_{P(\mathbf{z}|\mathbf{x},\mathbf{f},\Phi)} \left[\nabla_{\mathbf{f}} [\log P(\mathbf{z} | \mathbf{f})] \right] &= \mathbb{E}_{P(\mathbf{z}|\mathbf{x},\mathbf{f},\Phi)} \left[\nabla_{\mathbf{f}} \sum_{q=1}^{2n_z+1} \sum_{p=1}^{n_z} f_{q,p}(z_{q,p}) \right] \\ &\quad - \mathbb{E}_{P(\mathbf{z}|\mathbf{f})} \left[\nabla_{\mathbf{f}} \sum_{q=1}^{2n_z+1} \sum_{p=1}^{n_z} f_{q,p}(z_{q,p}) \right].\end{aligned}\tag{46}$$

A.6.5 Deriving the Thermodynamic Integral

Starting from the power posterior:

$$P(\mathbf{z} | \mathbf{x}^{(b)}, \mathbf{f}, \Phi, t) = \frac{P(\mathbf{x}^{(b)} | \mathbf{z}, \Phi)^t P(\mathbf{z} | \mathbf{f})}{\mathbf{Z}_t}\tag{47}$$

The partition function \mathbf{Z}_t is given by:

$$\mathbf{Z}_t = \mathbb{E}_{P(\mathbf{z}|\mathbf{f})} \left[P(\mathbf{x}^{(b)} | \mathbf{z}, \Phi)^t \right]\tag{48}$$

Now, differentiating the log-partition function with respect to t :

$$\begin{aligned}
\frac{\partial}{\partial t} \log(\mathbf{Z}_t) &= \frac{1}{\mathbf{Z}_t} \frac{\partial}{\partial t} \mathbf{Z}_t = \frac{1}{\mathbf{Z}_t} \mathbb{E}_{P(\mathbf{z}|\mathbf{f})} \left[\frac{\partial}{\partial t} P(\mathbf{x}^{(b)} | \mathbf{z}, \Phi)^t \right] \\
&= \frac{1}{\mathbf{Z}_t} \mathbb{E}_{P(\mathbf{z}|\mathbf{f})} \left[\log P(\mathbf{x}^{(b)} | \mathbf{z}, \Phi) \cdot P(\mathbf{x}^{(b)} | \mathbf{z}, \Phi)^t \right] \\
&= \mathbb{E}_{P(\mathbf{z}|\mathbf{x}^{(b)}, \mathbf{f}, \Phi, t)} \left[\log P(\mathbf{x}^{(b)} | \mathbf{z}, \Phi) \right]
\end{aligned} \tag{49}$$

Integrating both sides from 0 to 1:

$$\int_0^1 \frac{\partial}{\partial t} \log(\mathbf{Z}_t) dt = \int_0^1 \mathbb{E}_{P(\mathbf{z}|\mathbf{x}^{(b)}, \mathbf{f}, \Phi, t)} \left[\log P(\mathbf{x}^{(b)} | \mathbf{z}, \Phi) \right] dt \tag{50}$$

Using the fundamental theorem of calculus, presented by Larson and Edwards [2008]:

$$\int_0^1 \frac{\partial}{\partial t} \log(\mathbf{Z}_t) dt = \log(\mathbf{Z}_{t=1}) - \log(\mathbf{Z}_{t=0}) = \int_0^1 \mathbb{E}_{P(\mathbf{z}|\mathbf{x}^{(b)}, \mathbf{f}, \Phi, t)} \left[\log P(\mathbf{x}^{(b)} | \mathbf{z}, \Phi) \right] dt \tag{51}$$

The limits of the integrals can be expressed as:

$$\begin{aligned}
\log(\mathbf{Z}_{t=0}) &= \log \left(\mathbb{E}_{P(\mathbf{z}|\mathbf{f})} \left[P(\mathbf{x}^{(b)} | \mathbf{z}, \Phi)^0 \right] \right) = \log(1) = 0 \\
\log(\mathbf{Z}_{t=1}) &= \log \left(\mathbb{E}_{P(\mathbf{z}|\mathbf{x}^{(b)}, \mathbf{f}, \Phi)} \left[\log P(\mathbf{x}^{(b)} | \mathbf{z}, \Phi) \right] \right) = \log P(\mathbf{x}^{(b)} | \mathbf{f}, \Phi)
\end{aligned} \tag{52}$$

Therefore, we obtain the log-marginal likelihood expressed as the Thermodynamic Integral:

$$\log(\mathbf{Z}_{t=1}) - \log(\mathbf{Z}_{t=0}) = \log P(\mathbf{x}^{(b)} | \mathbf{f}, \Phi) = \int_0^1 \mathbb{E}_{P(\mathbf{z}|\mathbf{x}^{(b)}, \mathbf{f}, \Phi, t)} \left[\log P(\mathbf{x}^{(b)} | \mathbf{z}, \Phi) \right] dt \tag{53}$$

A.6.6 Learning gradient for discretized Thermodynamic Integral and power posterior partition function

We can derive the learning gradient of the discretized Thermodynamic Integral in Eq. 32 by reducing it down into a sum of normalizing constants. Starting from the definitions attributed to the KL divergence terms:

$$\begin{aligned}
D_{\text{KL}}(P_{t_{k-1}} \| P_{t_k}) &= \mathbb{E}_{P(\mathbf{z}|\mathbf{x}^{(b)}, \mathbf{f}, \Phi, t_{k-1})} \left[\log P(\mathbf{z} | \mathbf{x}^{(b)}, \mathbf{f}, \Phi, t_{k-1}) - \log P(\mathbf{z} | \mathbf{x}^{(b)}, \mathbf{f}, \Phi, t_k) \right] \\
\text{and } D_{\text{KL}}(P_{t_k} \| P_{t_{k-1}}) &= \mathbb{E}_{P(\mathbf{z}|\mathbf{x}^{(b)}, \mathbf{f}, \Phi, t_k)} \left[\log P(\mathbf{z} | \mathbf{x}^{(b)}, \mathbf{f}, \Phi, t_k) - \log P(\mathbf{z} | \mathbf{x}^{(b)}, \mathbf{f}, \Phi, t_{k-1}) \right] \\
&= -\mathbb{E}_{P(\mathbf{z}|\mathbf{x}^{(b)}, \mathbf{f}, \Phi, t_k)} \left[\log P(\mathbf{z} | \mathbf{x}^{(b)}, \mathbf{f}, \Phi, t_{k-1}) - \log P(\mathbf{z} | \mathbf{x}^{(b)}, \mathbf{f}, \Phi, t_k) \right]
\end{aligned} \tag{54}$$

We can leverage Eq. 30 to quantify the log-difference in terms of the change in likelihood contribution plus some normalization constant:

$$\log P(\mathbf{z} | \mathbf{x}^{(b)}, \mathbf{f}, \Phi, t_{k-1}) - \log P(\mathbf{z} | \mathbf{x}^{(b)}, \mathbf{f}, \Phi, t_k) = -\Delta t_k \cdot \log P(\mathbf{x}^{(b)} | \mathbf{z}, \Phi) + \log \left(\frac{\mathbf{Z}_{t_k}}{\mathbf{Z}_{t_{k-1}}} \right) \tag{55}$$

The definitions in Eq. 33 can be used to express the KL divergences in terms of the expected likelihoods:

$$\begin{aligned} \therefore D_{\text{KL}}(P_{t_{k-1}} \| P_{t_k}) &= -\Delta t_k \cdot \mathbb{E}_{P(\mathbf{z}|\mathbf{x}^{(b)}, \mathbf{f}, \Phi, t_{k-1})} \left[\log P(\mathbf{x}^{(b)} | \mathbf{z}, \Phi) \right] + \log \left(\frac{\mathbf{Z}_{t_k}}{\mathbf{Z}_{t_{k-1}}} \right) \\ &= -\Delta t_k \cdot E_{k-1} + \log \left(\frac{\mathbf{Z}_{t_k}}{\mathbf{Z}_{t_{k-1}}} \right) \end{aligned} \quad (56)$$

$$\begin{aligned} \text{and } D_{\text{KL}}(P_{t_k} \| P_{t_{k-1}}) &= \Delta t_k \cdot \mathbb{E}_{P(\mathbf{z}|\mathbf{x}^{(b)}, \mathbf{f}, \Phi, t_k)} \left[\log P(\mathbf{x}^{(b)} | \mathbf{z}, \Phi) \right] - \log \left(\frac{\mathbf{Z}_{t_k}}{\mathbf{Z}_{t_{k-1}}} \right) \\ &= \Delta t_k \cdot E_k - \log \left(\frac{\mathbf{Z}_{t_k}}{\mathbf{Z}_{t_{k-1}}} \right) \end{aligned} \quad (57)$$

Substituting back into Eq. 32, we eliminate the expected likelihood terms:

$$\begin{aligned} \frac{1}{2} \sum_{k=1}^{N_t} D_{\text{KL}}(P_{t_{k-1}} \| P_{t_k}) - D_{\text{KL}}(P_{t_k} \| P_{t_{k-1}}) &= -\frac{1}{2} \sum_{k=1}^{N_t} \Delta t_k (E_{k-1} + E_k) - 2 \log \left(\frac{\mathbf{Z}_{t_k}}{\mathbf{Z}_{t_{k-1}}} \right) \\ \therefore \log \left(P(\mathbf{x}^{(b)} | \mathbf{f}, \Phi) \right) &= \frac{1}{2} \sum_{k=1}^{N_t} \Delta t_k (E_{k-1} + E_k) + \frac{1}{2} \sum_{k=1}^{N_t} D_{\text{KL}}(P_{t_{k-1}} \| P_{t_k}) - D_{\text{KL}}(P_{t_k} \| P_{t_{k-1}}) \\ &= \frac{1}{2} \sum_{k=1}^{N_t} \Delta t_k (E_{k-1} + E_k) - \left[\frac{1}{2} \sum_{k=1}^{N_t} \Delta t_k (E_{k-1} + E_k) - 2 \log \left(\frac{\mathbf{Z}_{t_k}}{\mathbf{Z}_{t_{k-1}}} \right) \right] \\ &= \sum_{k=1}^{N_t} \log \left(\frac{\mathbf{Z}_{t_k}}{\mathbf{Z}_{t_{k-1}}} \right) = \sum_{k=1}^{N_t} \log(\mathbf{Z}_{t_k}) - \log(\mathbf{Z}_{t_{k-1}}) \end{aligned} \quad (58)$$

Following a similar method to Sec. A.6.4 we can use Eq. 40 to express the learning gradient attributed to each normalization constant in a simpler manner:

$$\begin{aligned} &\mathbb{E}_{P(\mathbf{z}|\mathbf{x}^{(b)}, \mathbf{f}, \Phi, t_k)} \left[\nabla_{\mathbf{f}, \Phi} \log P(\mathbf{z} | \mathbf{x}^{(b)}, \mathbf{f}, \Phi, t_k) \right] \\ &= \mathbb{E}_{P(\mathbf{z}|\mathbf{x}^{(b)}, \mathbf{f}, \Phi, t_k)} \left[t_k \cdot \nabla_{\Phi} \log P(\mathbf{x}^{(b)} | \mathbf{z}, \Phi) + \nabla_{\mathbf{f}} \log P(\mathbf{z} | \mathbf{f}) \right] - \nabla_{\mathbf{f}, \Phi} \log(\mathbf{Z}_{t_k}) = 0 \\ \therefore \nabla_{\mathbf{f}, \Phi} \log(\mathbf{Z}_{t_k}) &= \mathbb{E}_{P(\mathbf{z}|\mathbf{x}^{(b)}, \mathbf{f}, \Phi, t_k)} \left[t_k \cdot \nabla_{\Phi} \log P(\mathbf{x}^{(b)} | \mathbf{z}, \Phi) + \nabla_{\mathbf{f}} \log P(\mathbf{z} | \mathbf{f}) \right] \end{aligned} \quad (59)$$

Telescoping the sum in Eq. 58, and noting that $k = 1$ corresponds to the power posterior equaling the prior, and $k = N_t$ to the posterior, Eq. 58 yields T-KAM's learning gradient:

$$\begin{aligned} \nabla_{\mathbf{f}, \Phi} \log \left(P(\mathbf{x}^{(b)} | \mathbf{f}, \Phi) \right) &= \sum_{k=1}^{N_t} \nabla_{\mathbf{f}, \Phi} \log(\mathbf{Z}_{t_k}) - \nabla_{\mathbf{f}, \Phi} \log(\mathbf{Z}_{t_{k-1}}) \\ &= \nabla_{\mathbf{f}, \Phi} \log(\mathbf{Z}_{t_{N_t}}) - \nabla_{\mathbf{f}, \Phi} \log(\mathbf{Z}_{t_0}) \\ &= \mathbb{E}_{P(\mathbf{z}|\mathbf{x}^{(b)}, \mathbf{f}, \Phi)} \left[\nabla_{\mathbf{f}} \log P(\mathbf{z} | \mathbf{f}) + \nabla_{\Phi} \log P(\mathbf{x}^{(b)} | \mathbf{z}, \Phi) \right] \\ &\quad - \underbrace{\mathbb{E}_{P(\mathbf{z}|\mathbf{f})} \left[\nabla_{\mathbf{f}} [\log P(\mathbf{z} | \mathbf{f})] \right]}_{=0 \text{ (Eq. 40)}}. \end{aligned} \quad (60)$$

A.7 Sampling theory

This section provides more detail regarding T-KAM's sampling procedures.

A.7.1 Inverse transform sampling

We aim to draw samples from the component distribution $\pi_{q,p}$ defined in Eq. 4. Inverse transform sampling (ITS), as described by Devroye [2006], is a well-established method for generating high-quality samples. However, its application in high-dimensional settings is often impractical, especially in energy-based models with intractable partition functions.

T-KAM's unique properties, however, make it feasible. Specifically, the univariate and continuous nature of the prior components allows for efficient quadrature-based integral approximations.

Quadrature Integration

The spline functions $f_{q,p}$ are univariate, continuous, and defined on bounded grids spanning their domain, making quadrature approximations convenient for integrating each component. ITS requires the inversion of the cumulative distribution function (CDF) of the component distribution, which is defined as:

$$z_{q,p} = F^{-1}(\pi_{q,p})(u_p), \quad u_p \sim \mathcal{U}(u_p; 0, 1). \quad (61)$$

The cumulative distribution function (CDF) for $\pi_{q,p}$ is defined as:

$$F_{\pi_{q,p}}(z') = \frac{\int_{z_{\min}}^{z'} \exp(f_{q,p}(z)) \pi_0(z) dz}{Z_{q,p}}, \quad Z_{q,p} = \int_{z_{\min}}^{z_{\max}} \exp(f_{q,p}(z)) \pi_0(z) dz. \quad (62)$$

Both integrals can be approximated using Gauss-Konrad quadrature by Laurie [1997]:

$$\int_{z_{\min}}^{z'} G(z) dz \approx \sum_{i=1}^{N_{\text{quad}}} w_i G(z_i^{\text{node}}), \quad G(z) = \exp(f_{q,p}(z)) \pi_0(z), \quad (63)$$

where z_i^{node} and w_i are the Gauss-Legendre quadrature nodes and weights for the interval defined by $f_{q,p}$'s grid: $[z_{\min}, z']$. Gauss-Konrad nodes and weights can be obtained from existing software packages. For Gauss-Legendre they are defined on $[-1, 1]$, so the following affine transformation is applied to the nodes:

$$z_i^{\text{node}} = \frac{1}{2} \left((z' - z_{\min}) \cdot z_i^{[-1,1]} + (z' + z_{\min}) \right). \quad (64)$$

The corresponding weights are scaled by the Jacobian of the transformation:

$$w_i = w_i^{[-1,1]} \cdot \frac{z' - z_{\min}}{2}. \quad (65)$$

To invert the CDF, we must identify the quadrature index k^* such that:

$$k^* = \min \left\{ j \mid \sum_{i=1}^j w_i G(z_i^{\text{node}}) \geq Z_{q,p} \cdot u_p \right\}. \quad (66)$$

Linear Interpolation

The required sample lies within the trapezium bounded by $[z_{k^*-1}^{\text{node}}, z_{k^*}^{\text{node}}]$. To draw the sample $z_{q,p}$, we interpolate as follows:

$$z_{q,p} \approx z_{k^*-1}^{\text{node}} + (z_{k^*}^{\text{node}} - z_{k^*-1}^{\text{node}}) \cdot \frac{u_p - F_{\pi_{q,p}}(z_{k^*-1}^{\text{node}})}{F_{\pi_{q,p}}(z_{k^*}^{\text{node}}) - F_{\pi_{q,p}}(z_{k^*-1}^{\text{node}})}. \quad (67)$$

A.7.2 Importance Sampling

Importance Sampling (IS) is a Monte Carlo method rooted in the measure-theoretic formulation of probability. It enables the estimation of expectations with respect to one probability measure using samples drawn from another. For a detailed exposition, see Kloek and van Dijk [1978].

The Radon-Nikodym derivative

IS involves rewriting the expectation of an arbitrary function, $\rho(\mathbf{z})$, under the target measure, $P(\mathbf{z})$, in terms of a more tractable proposal measure, $Q(\mathbf{z})$. Specifically, we use the Radon-Nikodym derivative $\frac{dP}{dQ}$ to rewrite the expectation of an arbitrary function of \mathbf{z} , denoted as $\rho(\mathbf{z})$:

$$\mathbb{E}_{P(\mathbf{z})}[\rho(\mathbf{z})] = \int_{\bar{\mathcal{Z}}} \rho(\mathbf{z}) dP(\mathbf{z}) = \int_{\bar{\mathcal{Z}}} \rho(\mathbf{z}) \cdot \frac{dP}{dQ} dQ(\mathbf{z}). \quad (68)$$

Here, $\frac{dP}{dQ}$ acts as a weight that adjusts the contribution of each sample to account for the difference between the target and proposal measures. This requires that the proposal measure Q is absolutely continuous with respect to the target measure P , i.e. $Q(A) = 0$ implies $P(A) = 0$, for every measurable subset $A \in \mathcal{Z}$.

In the context of T-KAM, the target distribution is the posterior, $P(\mathbf{z} \mid \mathbf{x}^{(b)}, \mathbf{f}, \Phi)$, which is proportional to the product of the likelihood and the prior:

$$P(\mathbf{z} \mid \mathbf{x}^{(b)}, \mathbf{f}, \Phi) \propto P(\mathbf{x}^{(b)} \mid \mathbf{z}, \Phi) \cdot P(\mathbf{z} \mid \mathbf{f}). \quad (69)$$

The exact normalization constant, (the marginal likelihood $P(\mathbf{x}^{(b)} \mid \mathbf{f}, \Phi)$), is intractable, but Importance Sampling circumvents the need to compute it explicitly. Instead, the expectation of $\rho(\mathbf{z})$ under the posterior can be expressed as:

$$\mathbb{E}_{P(\mathbf{z} \mid \mathbf{x}^{(b)}, \mathbf{f}, \Phi)}[\rho(\mathbf{z})] = \int_{\bar{\mathcal{Z}}} \rho(\mathbf{z}) w(\mathbf{z}) dQ(\mathbf{z}), \quad (70)$$

where the importance weights $w(\mathbf{z})$ are given by:

$$w(\mathbf{z}) = \frac{P(\mathbf{z} \mid \mathbf{x}^{(b)}, \mathbf{f}, \Phi)}{Q(\mathbf{z})} = \frac{P(\mathbf{x}^{(b)} \mid \mathbf{z}, \Phi) \cdot P(\mathbf{z} \mid \mathbf{f})}{Q(\mathbf{z})}. \quad (71)$$

Proposal distribution and importance weights

A practical choice for the proposal distribution $Q(\mathbf{z})$ is the prior, $P(\mathbf{z} \mid \mathbf{f})$, given the availability of draws from the prior using the method outlined in Sec. A.7.1. This simplifies the importance weights, as the prior has a tractable form and covers the support of the posterior. This yields:

$$w(\mathbf{z}^{(s)}) = P(\mathbf{x}^{(b)} \mid \mathbf{z}^{(s)}, \Phi) \propto \exp(\log(P(\mathbf{x}^{(b)} \mid \mathbf{z}^{(s)}, \Phi))). \quad (72)$$

This reflects that the likelihood term now directly informs how much weight to assign to each sample \mathbf{z} . Intuitively, samples that better explain the observed data $\mathbf{x}^{(b)}$, (as measured by the likelihood), are given higher importance. Using the definition of softmax, the normalized weights are realizable as:

$$\frac{w(\mathbf{z}^{(s)})}{\sum_{r=1}^{N_s} w(\mathbf{z}^{(r)})} = \text{softmax}_s \left(\log(P(\mathbf{x}^{(b)} \mid \mathbf{z}^{(s)}, \Phi)) \right). \quad (73)$$

Resampling

The suitability of these weights depends on how well $Q(\mathbf{z})$ matches the posterior, ensuring a well-conditioned Radon-Nikodym derivative. In T-KAM, there is likely to be significant mismatch due to the complexity of the likelihood models described in Eq. 20. Consequently, the weights will exhibit high variance, resulting in many samples contributing minimally. This reduces the Effective Sample Size (ESS) and introduces bias into the estimates.

To address this, the weights are resampled before proceeding with the posterior expectation. This is accomplished by using one of the methods outlined by Douc et al. [2005], whenever the ESS falls below a certain threshold determined by Eq. 27. Resampling redistributes the sample weights, creating a new population with uniformly distributed weights while preserving the statistical properties of the original distribution. As training progresses and the prior becomes a better match for the posterior, the need for resampling decreases.

Importance Sampling estimator

To estimate the expectation, we draw N_s independent samples $\{\mathbf{z}^{(s)}\}_{s=1}^{N_s} \sim Q(\mathbf{z})$ using the procedure outlined in Sec. A.7.1 and compute a weighted sum:

$$\mathbb{E}_{P(\mathbf{z}|\mathbf{x}^{(b)}, \mathbf{f}, \Phi)}[\rho(\mathbf{z})] \approx \sum_{s=1}^{N_s} \rho(\mathbf{z}_{\text{resampled}}^{(s)}) \cdot w_{\text{norm, resampled}}(\bar{\mathbf{z}}_{\text{resampled}}^{(s)}),$$

$$\text{where } \mathbf{z}^{(s)} = \begin{pmatrix} (z_{1,1}^{(s)}, z_{1,2}^{(s)}, \dots, z_{1,n_z}^{(s)}) \\ (z_{2,1}^{(s)}, z_{2,2}^{(s)}, \dots, z_{2,n_z}^{(s)}) \\ \vdots \\ (z_{2n_z+1,1}^{(s)}, z_{2n_z+1,2}^{(s)}, \dots, z_{2n_z+1,n_z}^{(s)}) \end{pmatrix} \quad (74)$$

The estimator is unbiased, implying that its expectation matches the true posterior expectation. As $N_s \rightarrow \infty$, the approximation converges almost surely to the true value, provided that $Q(\mathbf{z})$ sufficiently covers the posterior to ensure a well-conditioned Radon-Nikodym derivative. This estimator is used for the log-marginal likelihood and its gradient in Eqs. 15 & 16, since it provides a means of estimating expectations with respect to the posterior distribution.

A.7.3 Residual resampling

In this study, we adopted residual resampling to redraw weights. This redistributes the population of latent samples according to the normalized weights of Sec. A.7.2. The procedure is only conducted when Eq. 27 regarding ESS is satisfied:

1. **Integer replication:** The sample, s , is replicated r_s times, where:

$$r_s = \lfloor N_s \cdot w_{\text{norm}}(\mathbf{z}^{(s)}) \rfloor \quad (75)$$

2. **Residual weights:** The total number of replicated samples after the previous stage will be $\sum_{s=1}^{N_s} r_s$. Therefore, $N_s - \sum_{s=1}^{N_s} r_s$ remain, which must be resampled using the residuals:

$$w_{\text{residual}}(\mathbf{z}^{(s)}) = w_{\text{norm}}(\mathbf{z}^{(s)}) \cdot (N_s - r_s)$$

$$w_{\text{norm, residual}}(\mathbf{z}^{(s)}) = \frac{w_{\text{residual}}(\mathbf{z}^{(s)})}{\sum_{s=1}^{N_s} w_{\text{residual}}(\mathbf{z}^{(s)})} \quad (76)$$

If a sample has been replicated at the previous stage, then its corresponding $w_{\text{norm, residual}}$ will be reduced, leading to a lower probability of it being resampled again.

3. **Resample:** The remaining samples are drawn with multinomial resampling, based on the cumulative distribution function of the residuals:

$$k^* = \min \left\{ j \mid \sum_{s=1}^j w_{\text{norm, residual}}(\mathbf{z}^{(s)}) \geq u_i \right\} \quad \text{where } u_i \sim \mathcal{U}([0, 1]). \quad (77)$$

where k^* represents the index of the sample to keep.

A.7.4 Metropolis-adjusted Langevin algorithm (MALA)

The Metropolis-Adjusted Langevin Algorithm (MALA), presented by Rosky et al. [1978] and Zhu and Mumford [1998], is a Markov Chain Monte Carlo (MCMC) method designed to sample from complex distributions by leveraging gradient information. It constructs a proposal mechanism that efficiently explores the target measure by combining stochastic perturbations with information from the target's local geometry to propose local moves, thereby refining the standard Metropolis-Hastings (MH) algorithm, outlined by Hastings [1970].

MALA operates on the target (power) posterior $P(\mathbf{z} \mid \mathbf{x}^{(b)}, \mathbf{f}, \Phi, t_k)$. The algorithm constructs a sequence of random variables $\{\mathbf{z}^{(i, t_k)}\}_{i=1}^{\infty}$ that forms a Markov chain converging in distribution to the target measure. The target posterior measure, $P(\mathbf{z} \mid \mathbf{x}^{(b)}, \mathbf{f}, \Phi, t_k)$, is:

$$\log P(\mathbf{z} \mid \mathbf{x}^{(b)}, \mathbf{f}, \Phi, t_k) = \log P(\mathbf{x}^{(b)} \mid \mathbf{z}, \Phi)^{t_k} + \log P(\mathbf{z} \mid \mathbf{f}) - \text{const}, \quad (78)$$

MALA

Starting with the initial state of the first chain, $\mathbf{z}^{(1, t_1)} \sim Q(\mathbf{z}) = P(\mathbf{z} \mid \mathbf{f})$, the local state within a temperature is updated as follows:

1. **Langevin diffusion:** A new state $\mathbf{z}'^{(i, t_k)}$ is proposed for a local chain, operating with a specific t_k , using a transition kernel inspired by (overdamped) Langevin dynamics, detailed by Roberts and Stramer [2002] and Brooks et al. [2011]:

$$\textbf{Target: } \log \gamma \left(\mathbf{z}'^{(i, t_k)} \right) \propto \log P(\mathbf{x}^{(b)} \mid \mathbf{z}, \Phi)^{t_k} + \log P(\mathbf{z} \mid \mathbf{f})$$

$$\textbf{Proposal: } \mathbf{z}'^{(i, t_k)} \mid \mathbf{z}^{(i, t_k)} \sim q \left(\mathbf{z}'^{(i, t_k)} \mid \mathbf{z}^{(i, t_k)} \right)$$

$$\textbf{Kernel: } q(\mathbf{z}'^{(i, t_k)} \mid \mathbf{z}^{(i, t_k)}) = \mathcal{N} \left(\mathbf{z}'^{(i, t_k)}; \mathbf{z}^{(i, t_k)} + \frac{\eta}{2} \mathbf{C} \cdot \nabla_{\mathbf{z}} \log \gamma \left(\mathbf{z}'^{(i, t_k)} \right), \left(\sqrt{\eta} \cdot \mathbf{C}^{\frac{1}{2}} \right)^2 \right), \quad (79)$$

where $\eta > 0$ is the step size, $\nabla_{\mathbf{z}} \log \gamma$ is the log-posterior gradient with respect to $\mathbf{z}^{(i, t_k)}$, and \mathbf{C} is a pre-conditioning, positive-definite matrix, (for example, the identity matrix, \mathbf{I}).

2. **MH criterion:** Once $N_{\text{unadjusted}}$ iterations have elapsed, Metropolis-Hastings adjustments, (MH by Metropolis and Ulam [1949]), are introduced. The MH criterion for the local proposal is:

$$r_{\text{local}} = \frac{\gamma \left(\mathbf{z}'^{(i, t_k)} \right) q \left(\mathbf{z}^{(i, t_k)} \mid \mathbf{z}'^{(i, t_k)} \right)}{\gamma \left(\mathbf{z}^{(i, t_k)} \right) q \left(\mathbf{z}'^{(i, t_k)} \mid \mathbf{z}^{(i, t_k)} \right)}, \quad (80)$$

3. **Acceptance:** The proposal is accepted with probability $\min(1, r_{\text{local}})$. If accepted, $\mathbf{z}^{(i+1, t_k)} = \mathbf{z}'^{(i, t_k)}$; otherwise, the current state is retained: $\mathbf{z}^{(i+1, t_k)} = \mathbf{z}^{(i, t_k)}$.
4. **Global Swaps:** Global swaps are proposed and accepted subject to the criterion outlined in Eq. 37

Convergence

Under mild regularity conditions, the local Markov chain $\{\mathbf{z}^{(i, t_k)}\}$ generated by MALA converges in distribution to $P(\mathbf{z} \mid \mathbf{x}^{(b)}, \mathbf{f}, \Phi, t_k)$ as $N_{\text{local}} \rightarrow \infty$. The proposal mechanism in Eq. 79 ensures that the chain mixes efficiently, particularly in high-dimensional spaces, provided that the step size η is tuned appropriately. The algorithm provides theoretical guarantees of the target, due to its satisfaction of detailed balance under Eq. 80:

$$\gamma \left(\mathbf{z}^{(i, t_k)} \right) q \left(\mathbf{z}'^{(i, t_k)} \mid \mathbf{z}^{(i, t_k)} \right) = \gamma \left(\mathbf{z}'^{(i, t_k)} \right) q \left(\mathbf{z}^{(i, t_k)} \mid \mathbf{z}'^{(i, t_k)} \right), \quad (81)$$

ensuring that the stationary distribution of the local chain matches the local target.

A.7.5 autoMALA

More details on the Metropolis-adjusted Langevin Algorithm (MALA) are provided in Sec. A.7.4.

Selecting an appropriate step size for unaltered MALA presents a challenge, particularly for SE, as each power posterior exhibits distinct local curvature. To address this, we adaptively tune the step size with autoMALA introduced by Biron-Lattes et al. [2024], which reinterprets MALA as Hamiltonian Monte Carlo (HMC) with a single leapfrog step, (introduced by Duane et al. [1987]).

The algorithm operates locally on a target power posterior $P(\mathbf{z} \mid \mathbf{x}^{(b)}, \mathbf{f}, \Phi, t_k)$. It constructs a sequence of random variables per temperature, $\{\mathbf{z}^{(i, t_k)}\}_{i=1}^{\infty}$, that forms a Markov chain converging in distribution to the local target:

$$\log \gamma \left(\mathbf{z}'^{(i, t_k)} \right) = \log P(\mathbf{z}^{(i, t_k)} \mid \mathbf{x}^{(b)}, \mathbf{f}, \Phi, t_k) \propto \log P(\mathbf{x}^{(b)} \mid \mathbf{z}^{(i, t_k)}, \Phi)^{t_k} + \log P(\mathbf{z}^{(i, t_k)} \mid \mathbf{f}).$$

Starting with the initial state of the first chain, $\mathbf{z}^{(1, t_1)} \sim Q(\mathbf{z}) = P(\mathbf{z} \mid \mathbf{f})$, the local state within a temperature is updated as follows:

1. **Acceptance thresholds:** Two bounding acceptance thresholds are sampled uniformly:

$$a, b \sim \mathcal{U}\left((a, b); \mathbf{0}, \mathbf{1}\right), \quad (a, b) \in [0, 1]^2, \quad b > a \quad (82)$$

2. **Mass matrix:** Random pre-conditioning matrices are initialized per latent dimension:

$$\varepsilon^{(i, t_k)} \sim \text{Beta}_{01}\left(1, 1; \left[\frac{1}{2}, \frac{2}{3}\right]\right),$$

$$M_{p,p}^{1/2 (i, t_k, q)} = \varepsilon^{(i, t_k)} \cdot \Sigma_{p,p}^{-1/2 (i, t_k, q)} + (1 - \varepsilon^{(i, t_k)}), \quad (83)$$

where $\Sigma_{p,p}^{(i, t_k, q)} = \text{VAR}_s \left[\tilde{z}_{q,p}^{(i, t_k, s)} \right]$. Here, $\text{Beta}_{01} [a, b; c, d]$ denotes a zero-one-inflated Beta distribution. The parameters $a, b > 0$ represent the shape parameters of the Beta distribution, while $c, d \in [0, 1]^2$ specify the probabilities governing the mixture. The positive definite mass matrix, M , can be related to Eq. 79 as $M = C^{-1}$, and is efficient to invert as a diagonal matrix.

3. **Leapfrog proposal:** The following transition is proposed for a local chain, t_k , with an adaptive step size, $\eta^{(i, t_k)}$:

$$\begin{aligned} \mathbf{p}^{(i, t_k)} &\sim \mathcal{N}\left(\mathbf{p}; \mathbf{0}, M^{(i, t_k)}\right) \\ \mathbf{p}'_{1/2}{}^{(i, t_k)} &= \mathbf{p}^{(i, t_k)} + \frac{\eta^{(i, t_k)}}{2} \nabla_{\mathbf{z}} \log \gamma\left(\mathbf{z}'^{(i, t_k)}\right) \\ \mathbf{z}'^{(i, t_k)} &= \mathbf{z}^{(i, t_k)} + \eta^{(i, t_k)} \left(M^{-1} \mathbf{p}'_{1/2}\right)^{(i, t_k)} \\ \hat{\mathbf{p}}^{(i, t_k)} &= \mathbf{p}'_{1/2}{}^{(i, t_k)} + \frac{\eta^{(i, t_k)}}{2} \nabla_{\mathbf{z}} \log \gamma\left(\mathbf{z}'^{(i, t_k)}\right) \\ \mathbf{p}'^{(i, t_k)} &= -\hat{\mathbf{p}}^{(i, t_k)}, \end{aligned} \quad (84)$$

4. **MH criterion:** Once $N_{\text{unadjusted}}$ iterations have elapsed, Metropolis-Hastings (MH) adjustments are introduced. The MH acceptance criterion for the local proposal is:

$$r_{\text{local}} = \frac{\gamma\left(\mathbf{z}'^{(i, t_k)}\right) \mathcal{N}\left(\mathbf{p}'^{(i, t_k)}; \mathbf{0}, M^{(i, t_k)}\right)}{\gamma\left(\mathbf{z}^{(i, t_k)}\right) \mathcal{N}\left(\mathbf{p}^{(i, t_k)}; \mathbf{0}, M^{(i, t_k)}\right)}, \quad (85)$$

5. **Step size adaptation:** Starting with an initial estimate, $\eta_{\text{init}}^{(i, t_k)}$, set as the average accepted step size from the previous training iteration, (used as a simple alternative to the round-based tuning algorithm proposed by Biron-Lattes et al. [2024]), the step size is adjusted as follows:

- If $a < r_{\text{local}} < b$, then $\eta^{(i, t_k)} = \eta_{\text{init}}^{(i, t_k)}$
- If $r_{\text{local}} \leq a$, then $\eta'{}^{(i, t_k)} = \eta_{\text{init}}^{(i, t_k)} / \Delta\eta^k$, where $k \leftarrow k+1$ is chosen recursively until $r_{\text{local}} > a$, and the step size is accepted, $\eta^{(i, t_k)} = \eta'{}^{(i, t_k)}$
- If $r_{\text{local}} \geq b$, then $\eta'{}^{(i, t_k)} = \eta_{\text{init}}^{(i, t_k)} \cdot \Delta\eta^k$, where $k \leftarrow k+1$ is chosen recursively until $r_{\text{local}} < b$, and the step size is accepted, $\eta^{(i, t_k)} = \eta'{}^{(i, t_k)} / \Delta\eta$

Here, $\Delta\eta$ is a tunable hyperparameter that controls the rate of step size adaptation. To improve efficiency in our implementation, tuning is prematurely terminated when $\eta^{(i, t_k)}$ falls out of a user-defined range, $[\eta_{\text{min}}, \eta_{\text{max}}]$. Excessively large or small step sizes are not beneficial, so preventing the algorithm from searching extreme values saves time without compromising performance.

6. **Reversibility check:** If the step size was modified, the reversibility of the update in Eq. 84 is verified before proceeding with MH acceptance. If $\eta_{\text{init}}^{(i, t_k)}$ cannot be recovered from the reversed step-size adjustment process with the proposed state, $\{\mathbf{z}'^{(i, t_k)}, \mathbf{p}'^{(i, t_k)}, \eta^{(i, t_k)}\}$, the proposal is rejected regardless of the outcome of the MH adjustment.

7. **Acceptance:** The proposal is accepted with probability $\min(1, r_{\text{local}})$. If accepted, $\mathbf{z}^{(i+1, t_k)} = \mathbf{z}'^{(i, t_k)}$; otherwise, the current state is retained: $\mathbf{z}^{(i+1, t_k)} = \mathbf{z}^{(i, t_k)}$.

8. **Global Swaps:** Global swaps are proposed and accepted subject to the criterion outlined in Eq. 37

A.8 20×20 image grids

A.8.1 MNIST

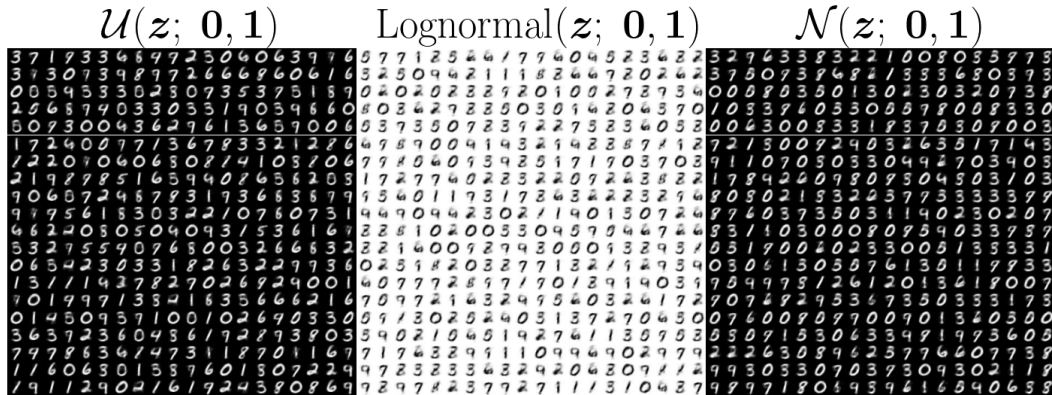


Figure 13: Generated MNIST, (Deng [2012]), after 2,000 parameter updates using MLE / IS adhering to KART’s structure. Uniform, lognormal, and Gaussian priors are contrasted using Radial Basis Functions, (Li [2024]). Lognormal is inverted for clarity.

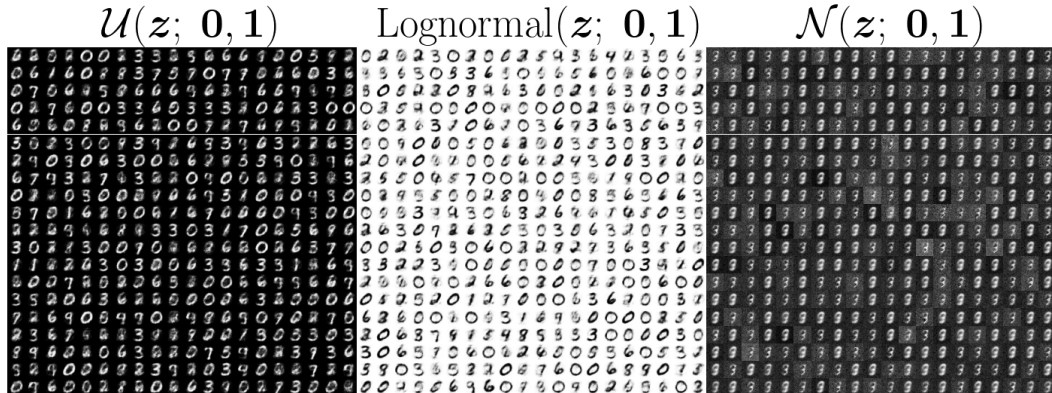


Figure 14: Generated MNIST, (Deng [2012]), after 2,000 parameter updates using MLE / IS adhering to KART’s structure. Uniform, lognormal, and Gaussian priors are contrasted using Fourier Bases, (Xu et al. [2024]). Lognormal is inverted for clarity.

A.8.2 FMNIST

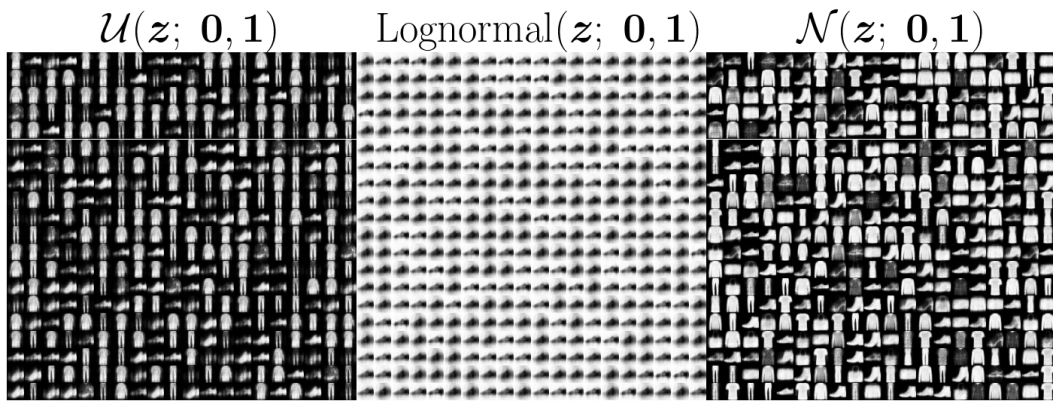


Figure 15: Generated FMNIST, (Xiao et al. [2017]), after 2,000 parameter updates using MLE / IS adhering to KART’s structure. Uniform, lognormal, and Gaussian priors are contrasted using Radial Basis Functions, (Li [2024]). Lognormal is inverted for clarity.

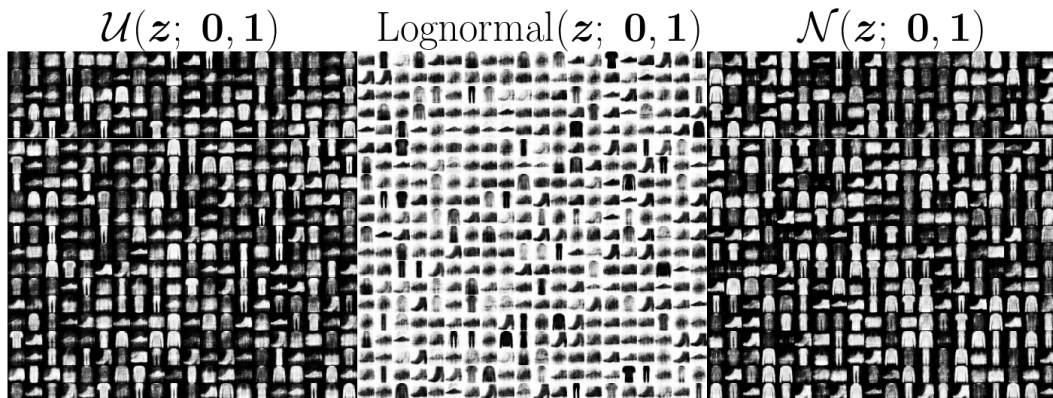


Figure 16: Generated FMNIST, (Xiao et al. [2017]), after 2,000 parameter updates using MLE / IS adhering to KART’s structure. Uniform, lognormal, and Gaussian priors are contrasted using Fourier Bases, (Xu et al. [2024]). Lognormal is inverted for clarity.

A.8.3 Darcy flow

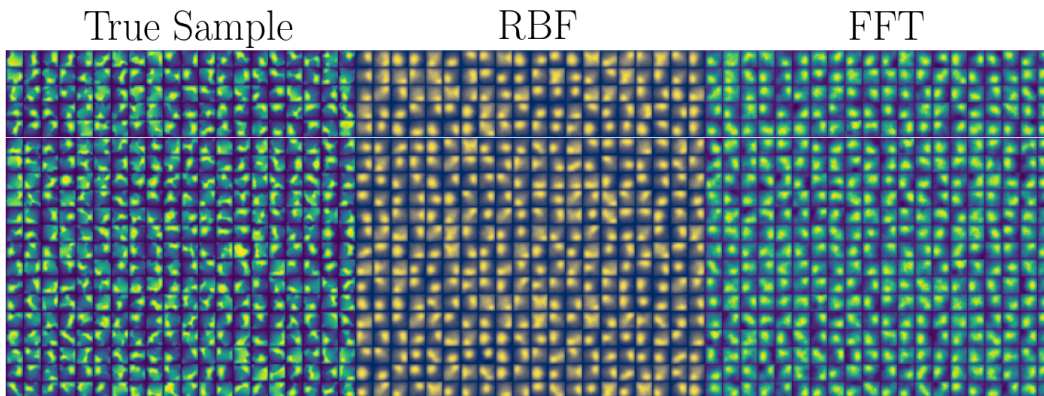


Figure 17: Generated 2D Darcy flow pressures, (Li et al. [2021]), after 12,000 parameter updates using MLE / IS while adhering to KART. Radial Basis Functions, (RBFs by Li [2024]), are contrasted against Fourier bases, (FFTs by Xu et al. [2024]), using Gaussian latent priors. RBF is colored differently for clarity.

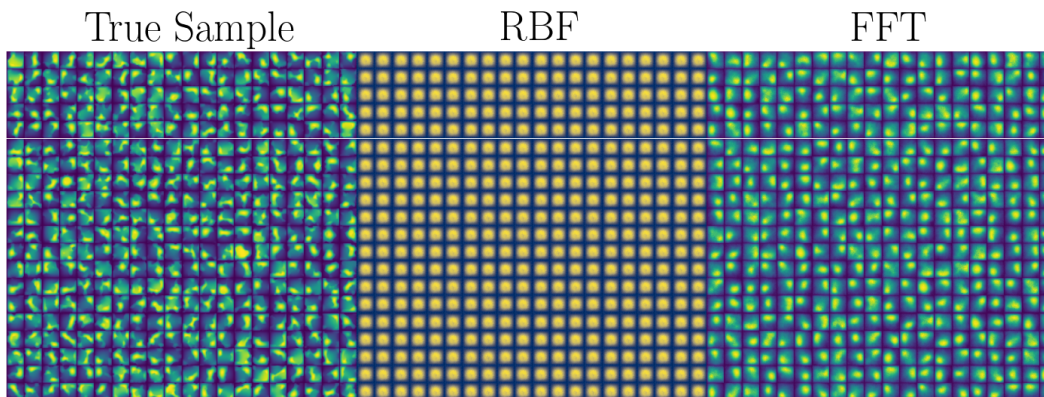


Figure 18: Generated 2D Darcy flow pressures, (Li et al. [2021]), after 12,000 parameter updates using MLE / IS while adhering to KART. Radial Basis Functions, (RBFs by Li [2024]), are contrasted against Fourier bases, (FFTs by Xu et al. [2024]), using lognormal latent priors. RBF is colored differently for clarity.

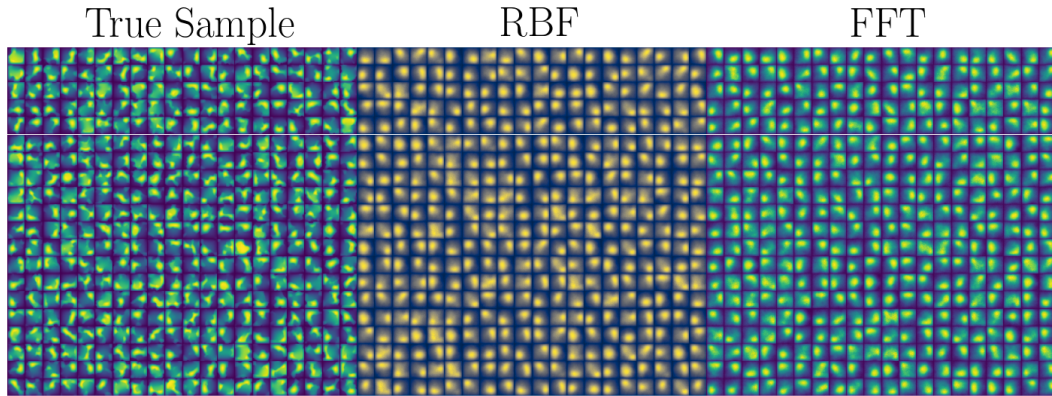


Figure 19: Generated 2D Darcy flow pressures, (Li et al. [2021]), after 12,000 parameter updates using MLE / IS while adhering to KART. Radial Basis Functions, (RBFs by Li [2024]), are contrasted against Fourier bases, (FFTs by Xu et al. [2024]), using uniform latent priors. RBF is colored differently for clarity.

A.8.4 SVHN



(a) SVHN with mixture prior and MLE

(b) SVHN with mixture prior and SE

Figure 20: Generated samples from T-KAM trained on SVHN using a mixture Chebyshev KAN prior, (SS et al. [2024]), after 8,000 parameter updates with ITS prior and ULA posterior sampling.

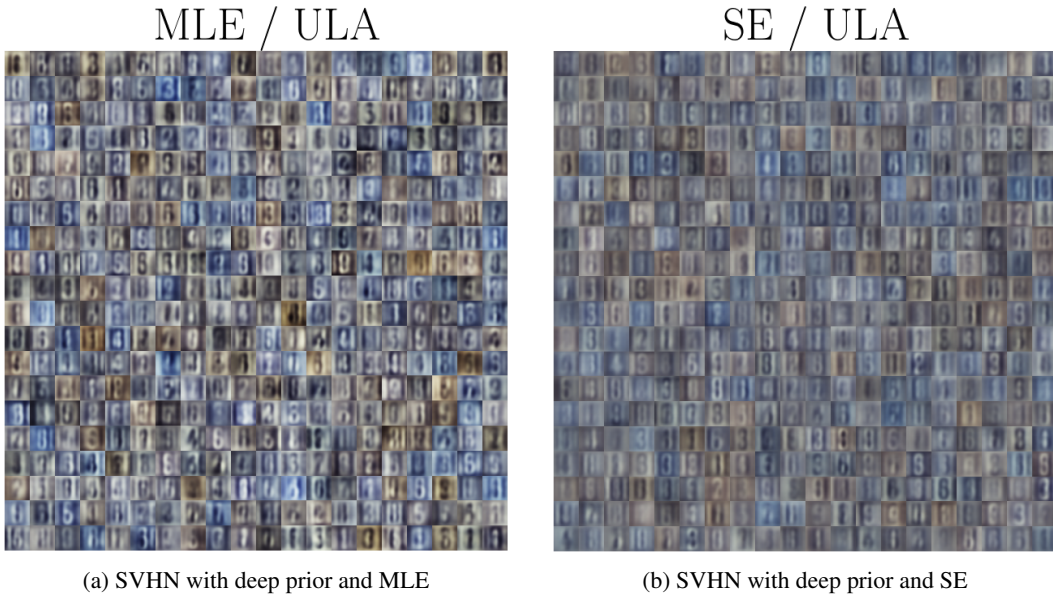


Figure 21: Generated samples from T-KAM trained on SVHN using a deep Chebyshev KAN prior, (SS et al. [2024]), after 8,000 parameter updates with ULA prior and ULA posterior sampling.

A.8.5 CIFAR-10

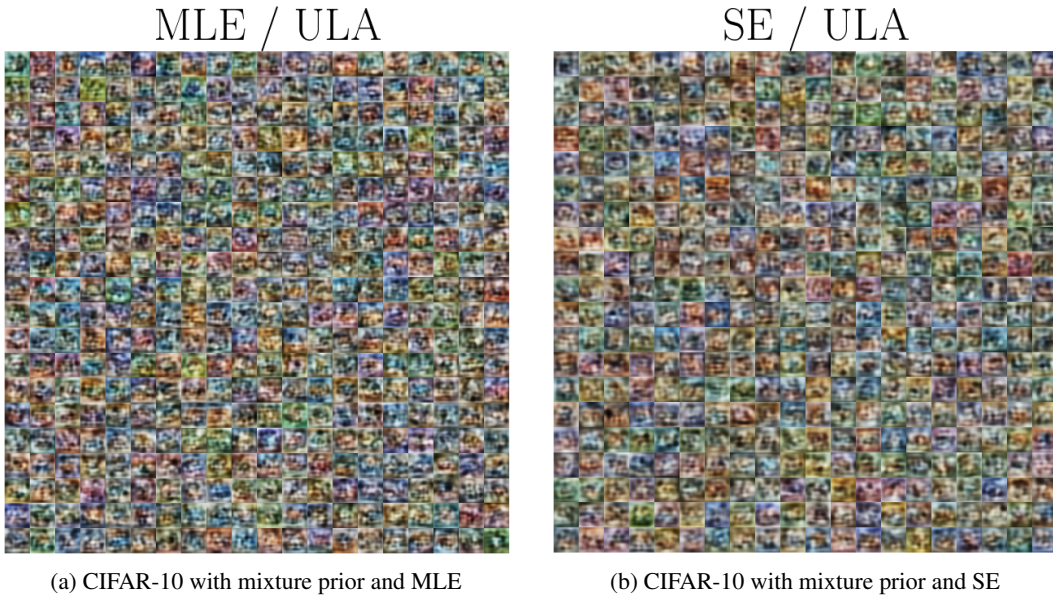


Figure 22: Generated samples from T-KAM trained on CIFAR-10 using a mixture Chebyshev KAN prior, (SS et al. [2024]), after 8,000 parameter updates with ITS prior and ULA posterior sampling.

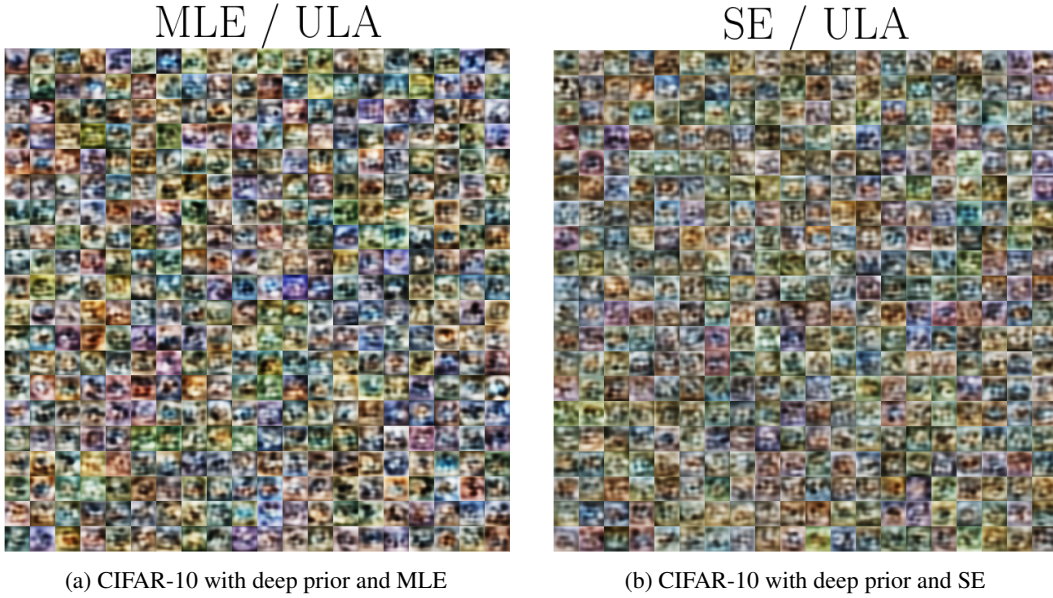


Figure 23: Generated samples from T-KAM trained on CIFAR-10 using a deep Chebyshev KAN prior, (SS et al. [2024]), after 8,000 parameter updates with ULA prior and ULA posterior sampling.

A.9 Top 3 extracted priors

The following priors were extracted from trained T-KAM models, each corresponding to the first three components of prior $q = 1$.

A.9.1 MNIST RBF

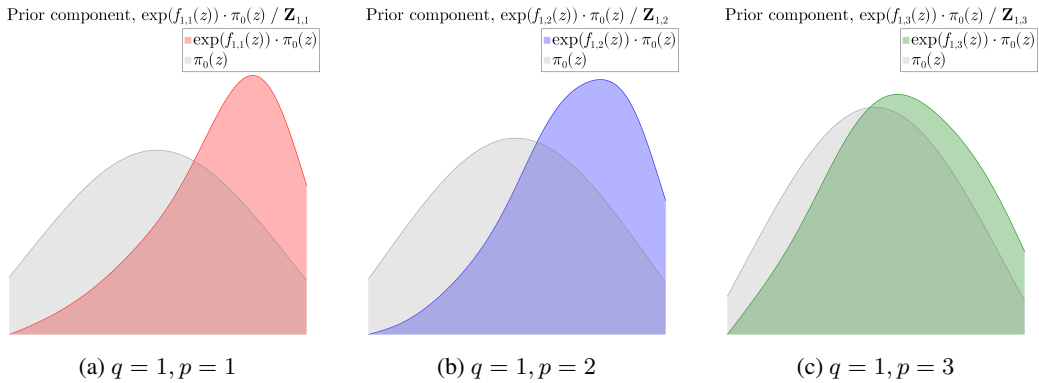


Figure 24: Three components from T-KAM’s prior after training on MNIST for 2,000 parameter updates with RBF bases and Gaussian constrained priors.

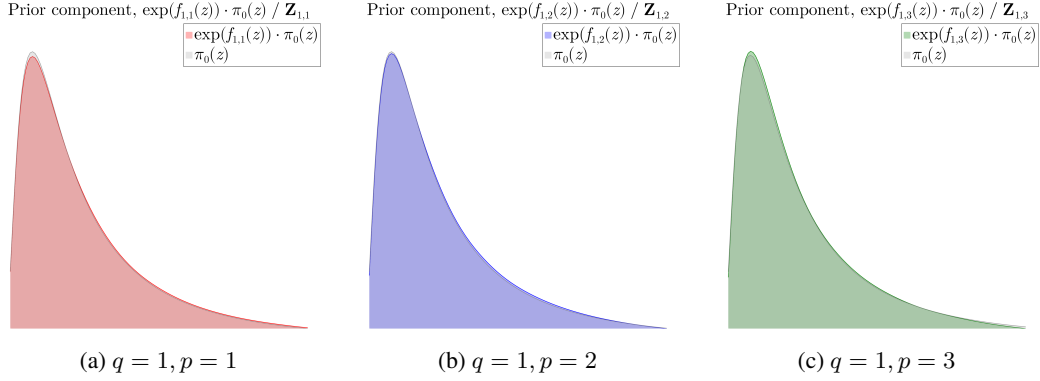


Figure 25: Three components from T-KAM's prior after training on MNIST for 2,000 parameter updates with RBF bases and lognormal constrained priors.

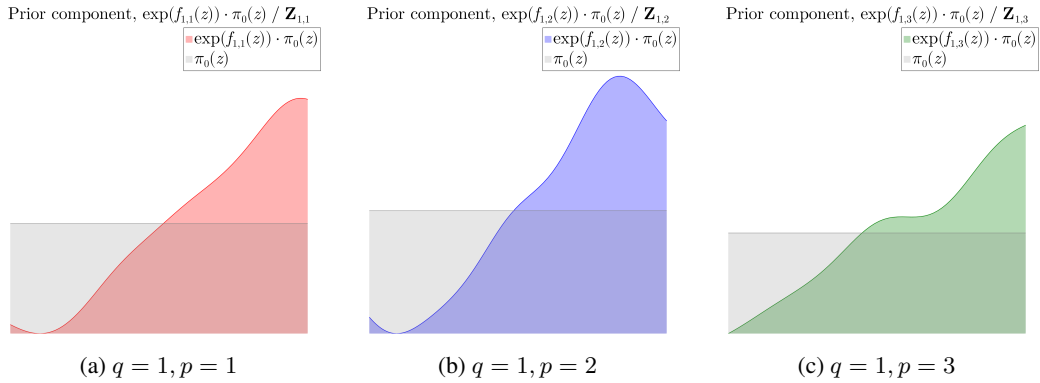


Figure 26: Three components from T-KAM's prior after training on MNIST for 2,000 parameter updates with RBF bases and uniform constrained priors.

A.9.2 MNIST FFT

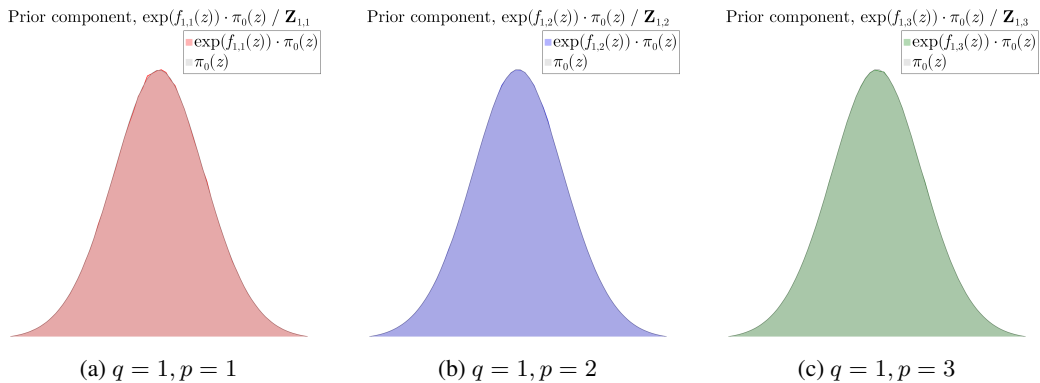


Figure 27: Three components from T-KAM's prior after training on MNIST for 2,000 parameter updates with FFT bases and Gaussian constrained priors.

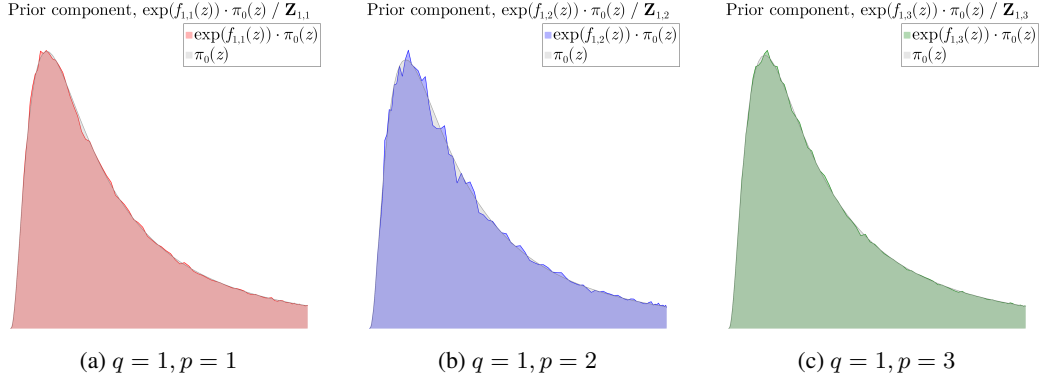


Figure 28: Three components from T-KAM's prior after training on MNIST for 2,000 parameter updates with FFT bases and lognormal constrained priors.

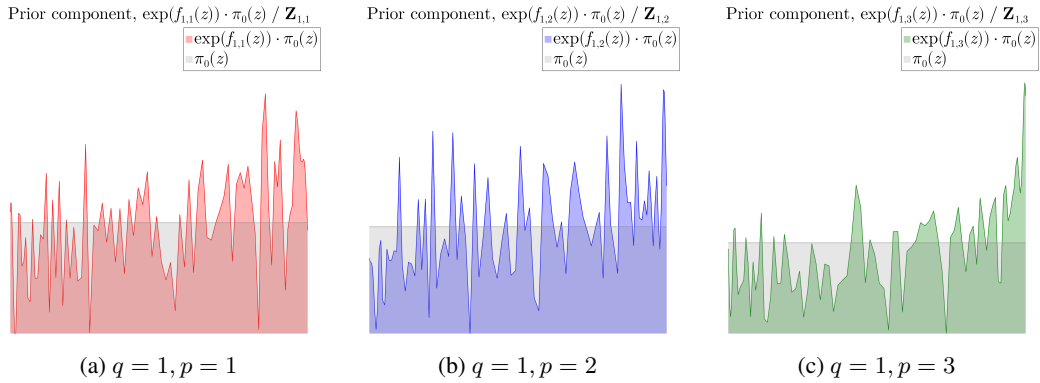


Figure 29: Three components from T-KAM's prior after training on MNIST for 2,000 parameter updates with FFT bases and uniform constrained priors.

A.9.3 FMNIST RBF

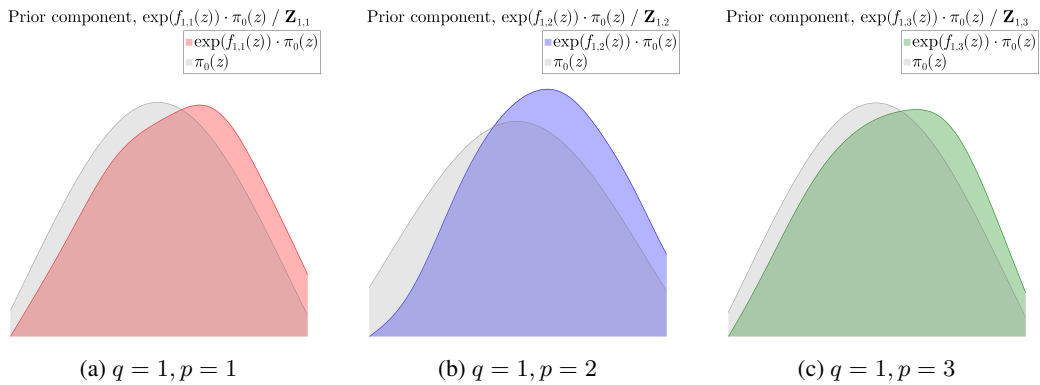


Figure 30: Three components from T-KAM's prior after training on FMNIST for 2,000 parameter updates with RBF bases and Gaussian constrained priors.

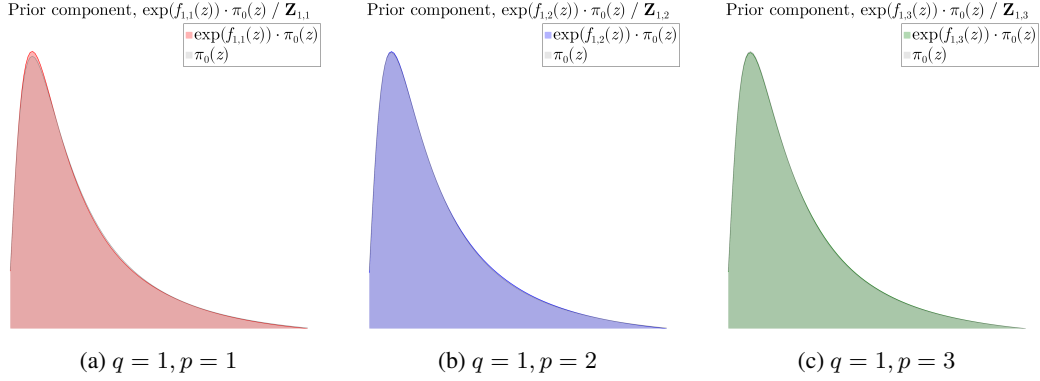


Figure 31: Three components from T-KAM's prior after training on FMNIST for 2,000 parameter updates with RBF bases and lognormal constrained priors.

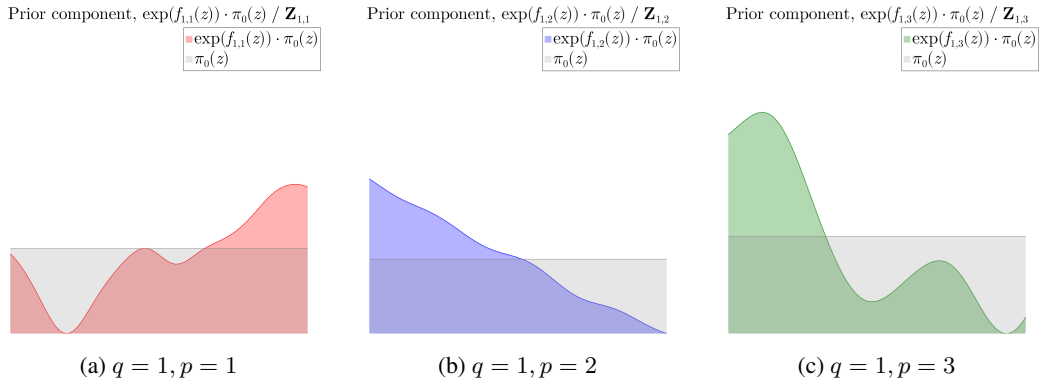


Figure 32: Three components from T-KAM's prior after training on FMNIST for 2,000 parameter updates with RBF bases and uniform constrained priors.

A.9.4 FMNIST FFT

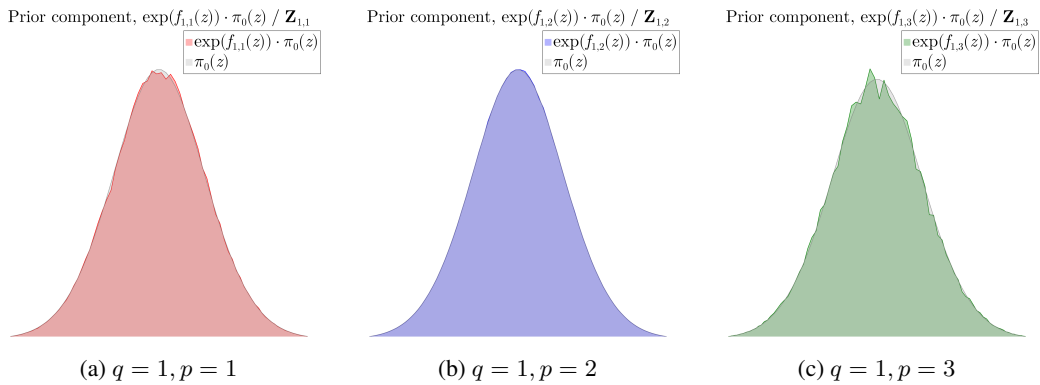


Figure 33: Three components from T-KAM's prior after training on FMNIST for 2,000 parameter updates with FFT bases and Gaussian constrained priors.

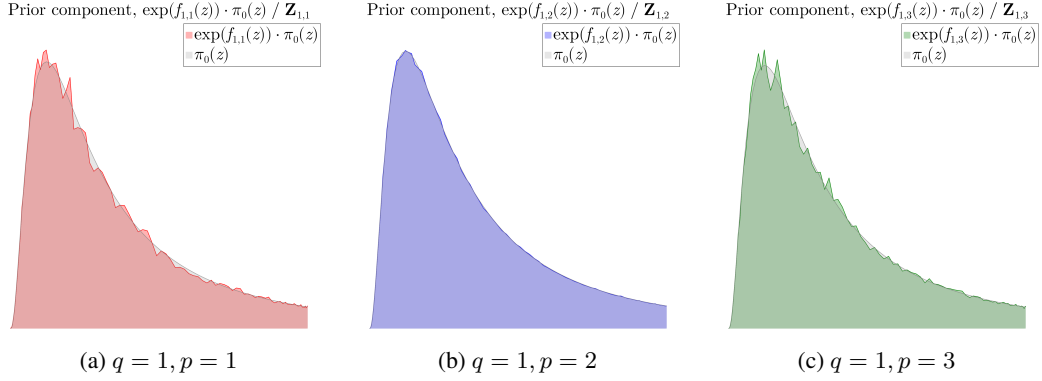


Figure 34: Three components from T-KAM's prior after training on FMNIST for 2,000 parameter updates with FFT bases and lognormal constrained priors.

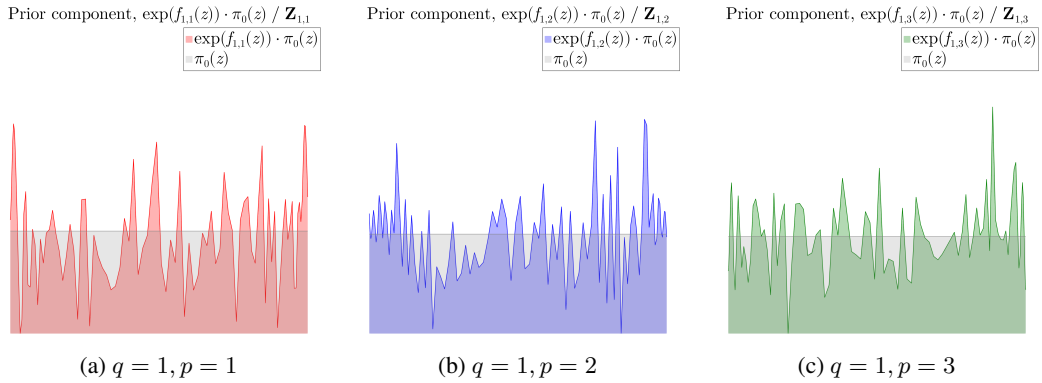


Figure 35: Three components from T-KAM's prior after training on FMNIST for 2,000 parameter updates with FFT bases and uniform constrained priors.

A.9.5 Darcy RBF

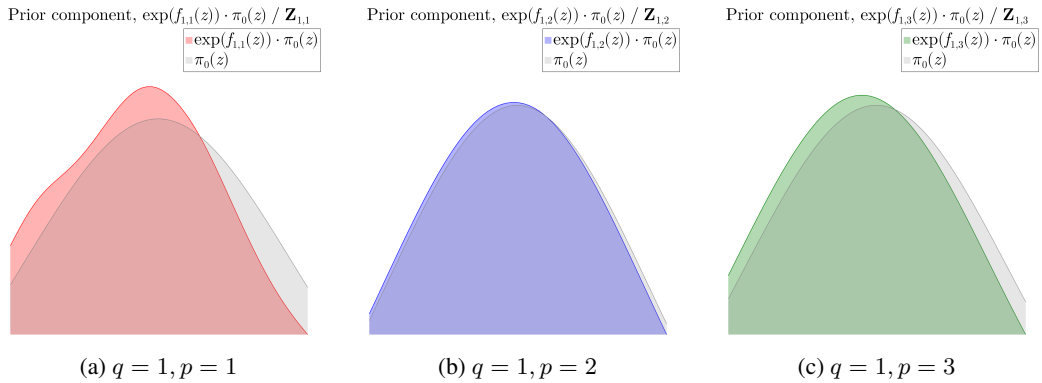


Figure 36: Three components from T-KAM's prior after training on Darcy flow pressures for 12,000 parameter updates with RBF bases and Gaussian constrained priors.

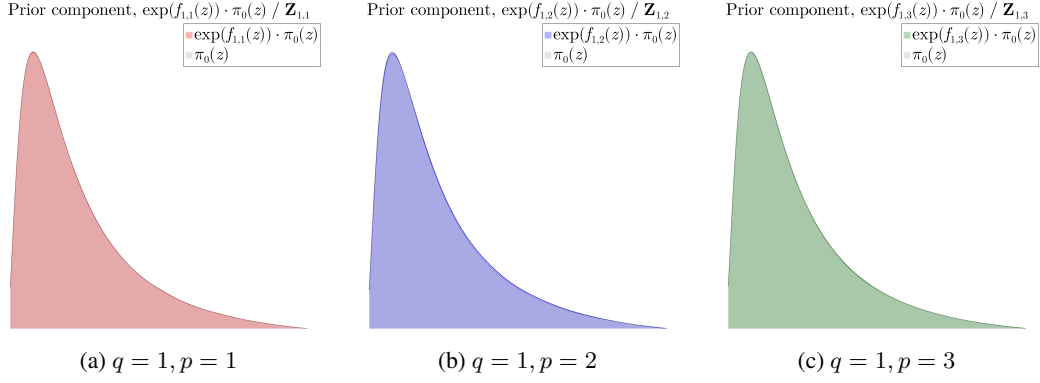


Figure 37: Three components from T-KAM's prior after training on Darcy flow pressures for 12,000 parameter updates with RBF bases and lognormal constrained priors.

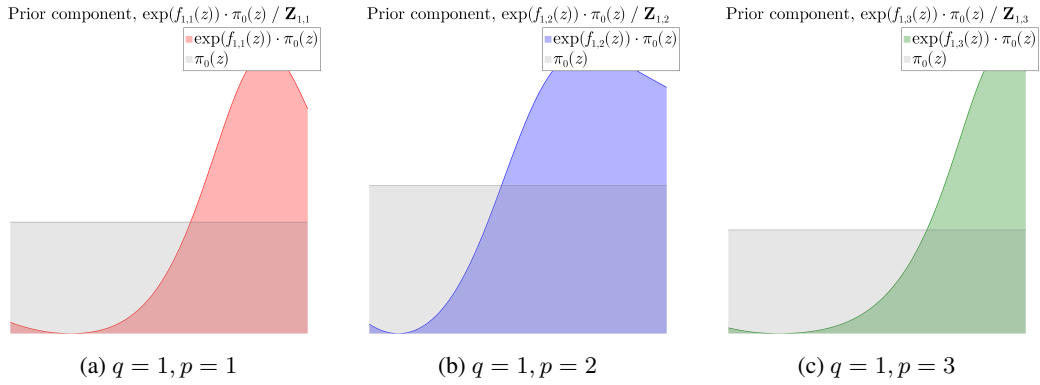


Figure 38: Three components from T-KAM's prior after training on Darcy flow pressures for 12,000 parameter updates with RBF bases and uniform constrained priors.

A.9.6 Darcy FFT

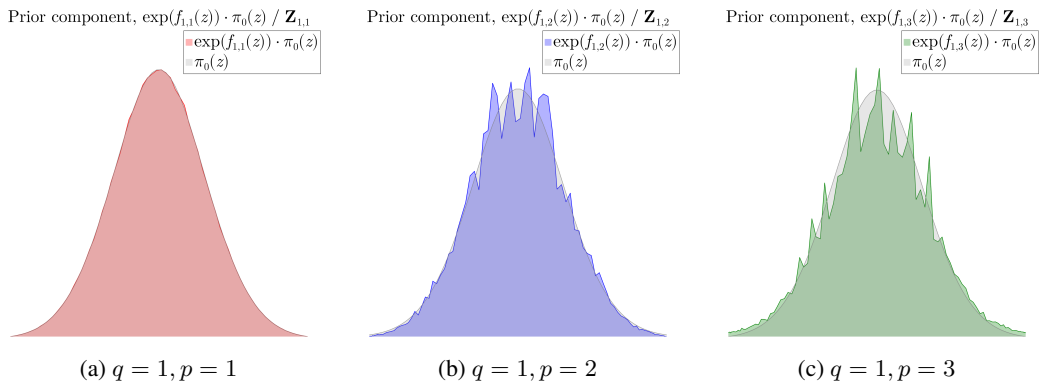


Figure 39: Three components from T-KAM's prior after training on Darcy flow pressures for 12,000 parameter updates with FFT bases and Gaussian constrained priors.

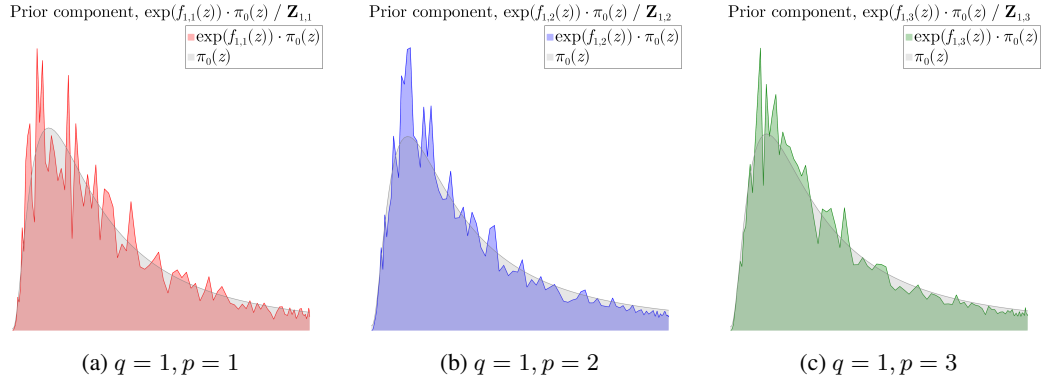


Figure 40: Three components from T-KAM's prior after training on Darcy flow pressures for 12,000 parameter updates with FFT bases and lognormal constrained priors.

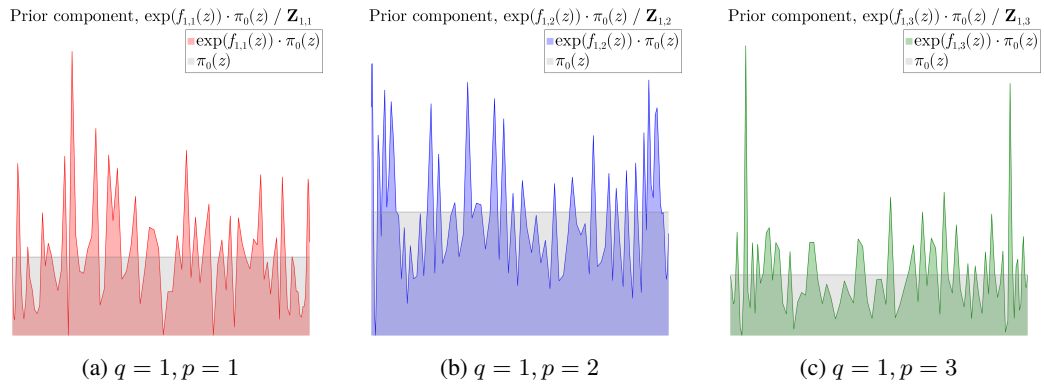


Figure 41: Three components from T-KAM's prior after training on Darcy flow pressures for 12,000 parameter updates with FFT bases and uniform constrained priors.